

A generalized mathematical model of geostrophic adjustment and frontogenesis: uniform potential vorticity

Callum J. Shakespeare and J. R. Taylor†

Department of Applied Mathematics and Theoretical Physics, University of Cambridge,
Centre for Mathematical Sciences, Wilberforce Road, Cambridge CB3 0WA, UK

(Received 20 March 2013; revised 27 September 2013; accepted 30 September 2013;
first published online 6 November 2013)

Fronts, or regions with strong horizontal density gradients, are ubiquitous and dynamically important features in the ocean and atmosphere. In the atmosphere, fronts are associated with some of the most severe weather events, while in the ocean, fronts are associated with enhanced turbulence, water mass transformation and biological activity. Here, we examine the dynamics involved in the formation of fronts, or frontogenesis, in detail using a generalized mathematical framework. This extends previous work which has generally revolved around two limiting cases: fronts generated through forcing due to a convergent large-scale flow, and fronts generated spontaneously during the geostrophic adjustment of an initially unbalanced flow. Here, we introduce a new generalized momentum coordinate to simultaneously describe forced and spontaneous frontogenesis. The nonlinear, inviscid, Boussinesq, hydrostatic governing equations for uniform PV flow are solved for arbitrary Rossby and Froude number. The solution is then examined in three distinct cases. Firstly, for a zero potential vorticity (PV) flow bounded by rigid lids, a general solution is derived for the transient response of the fluid to an arbitrary initial mass imbalance and deformation field. The deformation frontogenesis solution of Hoskins & Bretherton (*J. Atmos. Sci.*, vol. 29, 1972, pp. 11–37) and the mass imbalance solution of Blumen (*J. Phys. Oceanogr.*, vol. 30, 2000, pp. 31–39) emerge as two limits of this general solution. Secondly, the problem of geostrophic adjustment of an initial mass imbalance (no deformation field) is considered for uniform PV flow bounded by rigid lids. The general solution is derived, composed of an adjusted state and a transient component describing the propagation of inertia–gravity waves. The criteria for the occurrence of a frontal discontinuity is determined in terms of the Rossby and Froude numbers. The uniform PV solution reduces identically to the zero PV solution of Blumen in the limit of vanishing background stratification. Thirdly, we examine the more general case of uniform PV flow with a deformation field and either balanced or unbalanced initial conditions. In this case the solution is composed of a time-varying mean state – matching the Hoskins & Bretherton solution in the limit of small strain – and an inertia gravity wave field, the dynamics of which are examined in detail. Our analysis provides a unifying framework capable of describing frontal formation and geostrophic adjustment in a wide variety of settings.

Key words: atmospheric flows, ocean circulation, waves in rotating fluids

† Email address for correspondence: J.R.Taylor@damtp.cam.ac.uk

1. Introduction

Sharp horizontal density contrasts, or fronts, are ubiquitous features of the upper ocean, and the lower and upper troposphere. Fronts are familiar features at the edges of weather systems, and are often associated with precipitation and/or strong winds. There is evidence that fronts are capable of moderating the exchange of heat, carbon dioxide, and other fluid properties between the ocean and atmosphere (Ferrari 2011), thereby impacting the climate system on longer time scales. However, due to their small scales, fronts are often unresolved in climate simulations. Improving our understanding of the formation and dynamics of fronts will be an important step in advancing our ability to successfully model the coupled ocean/atmosphere system.

Direct observation of atmospheric fronts has revealed a wide range of behaviours and scales. Perhaps the most well known are synoptic-scale fronts of $O(1000\text{ km})$ in length, associated with large-scale atmospheric high and low pressure systems. These fronts are distinctive elongated features of near-surface temperature and wind fields typically associated with severe weather events. Synoptic fronts start as regions of weak temperature gradients on growing nonlinear baroclinic waves (Hoskins 1982). A variety of processes, such as local horizontal strain fields, velocity shears or differential diabatic heating, can act to intensify these temperature gradients, a process known as *frontogenesis* (Hoskins & Bretherton 1972). Frontogenesis drives a secondary circulation with upwelling on the warmer side of the front and downwelling on the cooler side, and a strengthened surface wind field. Atmospheric fronts are classed as cold fronts when the cold air mass is advancing into a region of warmer air. Cold fronts are typically responsible for the most severe weather events due to the intense upwelling of warm moist air ahead of the front driving substantial precipitation. However, synoptic scale fronts are only one member of a vast family of atmospheric frontal systems. For example, Blumen *et al.* (1996) describe a mesoscale cold front $O(100\text{ km})$ in length that exhibits very rapid sharpening to a step-like state in only a few hours. Understanding the evolution of such smaller-scale frontal systems is an area of ongoing research (e.g. Plougonven & Zeitlin 2005).

The deep ocean acts as a significant reservoir for heat and carbon, but the transfer of fluid properties from the surface to the deep ocean is strongly inhibited by the pervasive stable density stratification in the ocean interior. In the ocean, fronts are regions where isopycnals outcrop from the stratified interior to the surface. By forming an along-isopycnal connection between the surface and the ocean interior, and by enhancing local vertical velocities and mixing, ocean fronts may provide a conduit for the transfer of heat and other fluid properties between the surface and ocean interior (Ferrari 2011). Recent work suggests that fronts influence important processes in the ocean including mode water formation (Thomas & Joyce 2010; Thomas *et al.* 2013) and biological primary productivity (Taylor & Ferrari 2011; Mahadevan *et al.* 2012).

As already noted, frontogenesis is the process by which relatively weak horizontal density gradients are intensified. Two dynamical mechanisms driving this intensification which have received considerable attention in the literature are forcing by large-scale strain fields, and the geostrophic adjustment of fluid from an initially unbalanced state. We will refer to these two mechanisms as ‘forced’ and ‘spontaneous’ frontogenesis, respectively. One of the primary objectives of this work is to combine forced and spontaneous frontogenesis into a single, unified mathematical framework. Our model will include nonlinear effects and, unlike most previous models, the solution will be valid at arbitrary strain rates and Froude numbers.

Geostrophic adjustment refers to the adaptation of a rotating fluid system to an imposed force and/or set of initial conditions. This adjustment process is ubiquitous in the surface layers of both the atmosphere and ocean which are subject to rapid (compared to the inertial period) inputs of buoyancy and momentum. For example, in the adjustment problem considered by Rossby (1938), wind stress applied to the ocean causes a rapid acceleration of the surface layer resulting in an unbalanced Coriolis force (a momentum imbalance), and thus driving a change in the free surface height. In a related problem, a sudden change in the buoyancy of a fluid layer, for example in response to an air/sea flux of heat or fresh water, or a river outflow, will cause an unbalanced pressure field and thereby generate a flow that restratifies the layer (Tandon & Garrett 1994). For a relatively weak imbalance, the final state is in geostrophic balance. However, for larger imbalances significant questions arise as to whether: (i) a geostrophically balanced state exists; and (ii) if it does exist, whether it is attainable (Plougonven & Zeitlin 2005). For example, sufficiently large imbalances may lead to the spontaneous formation of a sharp front during the adjustment process (hence the name *spontaneous* frontogenesis). These issues have been the focus of significant research since Rossby's (1938) paper and yet remain largely unresolved in the general case.

Frontogenesis can also be triggered when an initially balanced flow is subject to an external force or acceleration. This process may be considered as one of *continuous geostrophic adjustment* (Plougonven & Zeitlin 2005) whereby the imposed force continually pushes the system away from geostrophic balance, and a secondary circulation acts to continually maintain geostrophic balance (and thus the system remains close to a balanced state throughout the process, if the imposed force is sufficiently small). An example of such a force is the horizontal convergence of flow in the region between weather systems or ocean eddies (e.g. Hoskins & Bretherton 1972, hereafter, HB72). The convergent flow amplifies pre-existing buoyancy gradients and thus drives the flow away from geostrophic balance. The resulting change in the pressure gradient generates a smaller-scale secondary circulation acting to restore geostrophic balance. However, nonlinear self-advection of this ageostrophic flow drives additional frontogenesis. In the model constructed by HB72, the combination of large-scale strain and secondary circulation leads to the formation of a discontinuity in the (inviscid) momentum and buoyancy fields in a finite period of time (HB72).

Many of the previous studies of frontogenesis have considered quasi-two-dimensional flow between rigid boundaries, where gradients in one direction (along-front) are neglected relative to the other (cross-front) direction. This configuration is applicable to straight fronts, where the variations in the along-front direction are generally on much larger scales than those in the cross-front direction. This approximation significantly aids the analysis. Early models (Sawyer 1956; Eliassen 1959) used this configuration to study cross-front motion in a large-scale geostrophic flow. A common assumption made in such models is that of semigeostrophy; that is, the assumption of purely geostrophic along-front flow. These two approximations led to the derivation of the diagnostic Sawyer–Eliassen equation describing the response of secondary frontal circulation to a large-scale geostrophic flow. Consistent with observations, the Sawyer–Eliassen equation predicted that a convergent large-scale strain field drives a secondary circulation consisting of upwelling on the warmer side of a front and downwelling on the cooler side.

A further key breakthrough occurred with the introduction of a new momentum coordinate system by Eliassen (1962) allowing analysis of nonlinear effects. The action of the geostrophic flow in tilting surfaces of absolute momentum $\mathcal{M} = fx + v$

was observed to cause sharpening of cross-front gradients near boundaries. HB72 employed the momentum coordinate system in a semigeostrophic model to determine a predictive equation for the evolution of a front in a large-scale deformation field converging towards the along-front axis. It was shown that any arbitrarily weak buoyancy gradient in the cross-front direction will form a discontinuity in finite time. In the HB72 model the frontal discontinuity emerges via a vanishing inverse Jacobian of the momentum coordinate transformation.

Frontogenesis driven by large-scale forcing (as described above) has largely been studied in isolation from the parallel problem of spontaneous frontogenesis associated with an initial mass or momentum imbalance. This is at least in part due to the analytical intractability of the latter problem, since the unbalanced initial conditions prohibit the use of quasi- or semigeostrophy, which both implicitly assume a degree of balance to the flow. The first attempts at solving the spontaneous frontogenesis problem mostly dealt with one-dimensional flow (see the review paper of Blumen 1972) until Ou (1984), who demonstrated that, in the case of initially motionless two-dimensional flow trapped between rigid boundaries, a continuous geostrophically adjusted state will not exist if the initial buoyancy gradient (mass imbalance) is sufficiently large. This result was further developed by Blumen & Wu (1995), who applied the Eliassen (1962) momentum coordinates to the mass imbalance problem to determine a general solution for the adjusted steady state in the special case of uniform potential vorticity (PV) flow. The similarity of their mathematical approach to that of HB72 emphasizes the connection between the spontaneous mass imbalance and forced frontogenesis problems – a fact also reflected on by Plougonven & Zeitlin (2005), and further explored in this work. Blumen & Wu (1995) did not use their result to determine the values of the Rossby and Froude numbers required for the existence of the adjusted state, or consider the temporal evolution. Here, we will examine both of these aspects in detail.

Plougonven & Zeitlin (2005) applied a Lagrangian approach to the problem of geostrophic adjustment of a frontal imbalance, with particular emphasis on the existence and attainability of an adjusted state. They found that the non-existence of the adjusted state is a generic property of bounded domains and that (expanding upon the results of Wu & Blumen 1995) frontogenesis is enhanced by the presence of an initial cyclonic horizontal shear. Thus, smaller imbalances can lead to spontaneous frontogenesis, meaning that the formation of mesoscale fronts in the atmosphere is likely to be a more common process than previously believed. The Plougonven & Zeitlin (2005) Lagrangian approach also illustrates the dynamical splitting of the fluid response into balanced (adjusted state) and unbalanced (inertia–gravity waves) motions. They emphasized the importance of the fully nonlinear unbalanced motions in determining whether the system can attain the adjusted state.

As observed by Blumen (2000, hereafter B00), most previous models have either not considered the transient motion but retained nonlinearity (e.g. Ou 1984; Blumen & Wu 1995), or included transient motion but neglected nonlinear effects (e.g. Tandon & Garrett 1994). While the time-independent equations can be used to determine the existence (or otherwise) of a geostrophically adjusted state, they cannot describe the transient adjustment process and hence the attainability of the adjusted state. For example, transient phenomena such as hydrodynamic instabilities, trapped waves, and propagating inertia–gravity waves may prevent the adjusted state from being reached. As a case in point, the model of B00 was the first to include both nonlinearity and time dependence to derive a general solution for the rigid lid mass imbalance problem in the special case of zero PV flow. The B00 solution consists of a non-

decaying inertial oscillation about a steady adjusted state – but the system never attains this adjusted state. The waves are effectively trapped, since the absence of a free surface or background stratification eliminates possible propagation mechanisms. The addition of density stratification will fundamentally alter the dynamics by permitting the propagation of inertia–gravity waves away from the frontal zone and hence allow the system to attain a steady state. However, no solution for the transient response to a mass imbalance in uniform PV flow (that is, the time-dependent motion pertaining to the attainment of the adjusted state determined by Blumen & Wu 1995) as yet exists.

The need for a unified description of frontogenesis that describes arbitrary initial conditions, non-zero PV and a wider range of time scales is becoming apparent as the study of geophysical phenomena moves to increasingly smaller scales, which have order-one Rossby and Froude numbers and evolve on shorter time scales. The time scale associated with the strain flow is the inverse strain rate $1/\alpha$, compared with the inertial time scale $1/f$ for the smaller-scale motion, which is dominated by inertia–gravity waves. The assumption made in the HB72 model is that the inertial time scale is much shorter than the strain time scale, or $\alpha/f \ll 1$. The ratio $\alpha/f = U/(fL)$ with flow speed $U \sim \alpha L$ for a length scale L may also be interpreted as the Rossby number pertaining to the large-scale flow, and hence HB72 may be characterized equivalently as a small-Rossby-number or large-time-scale theory.

Historically, the primary focus of research has been on synoptic-scale weather systems in the atmosphere or mesoscale eddies in the ocean. Since these systems are characterized by time scales that are long relative to the inertial period, approximations such as semigeostrophy are capable of describing the early stages of frontogenesis. More recently it has become apparent that smaller-scale eddies and fronts, collectively known as submesoscales, are common features of the upper ocean. In the ocean, the question of how submesoscale fronts in the surface mixed layer form, evolve, and break down is relevant to many important problems, including ocean biology (Ferrari 2011; Taylor & Ferrari 2011) and the oceanic energy cascade (Thomas, Tandon & Mahadevan 2008). However, since submesoscales are associated with shorter time scales (e.g. α/f order-one) and potentially unbalanced initial conditions, a dynamical description of submesoscale frontogenesis requires an extension of the HB72 theory.

With the above context in mind, we pose the major objectives of the present work as follows. First, we will seek to unify the deformation field theory of HB72 and the mass imbalance theory of B00 into a single model for the special case of uniform PV flow. This will be achieved via the introduction of a new coordinate system – a generalization of the momentum coordinates of Eliassen (1962). The classical theories of HB72 and B00 will emerge as two limits of a single consistent solution

In addition to demonstrating the dynamical similarity of mass imbalance and deformation frontogenesis, the generalized model developed here will extend previous work in several ways. In the absence of a deformation field, the generalized model will extend the work of B00 and Blumen & Wu (1995) by describing the transient response of a fluid with non-zero uniform PV to a mass imbalance. Previously, Blumen & Wu (1995) described only the steady state fields for this configuration and not the transient part of the flow, while B00 considered the transient response in the special case of zero PV. When a deformation field is included, the generalized model will extend the work pioneered by HB72 beyond the restrictions of the semi-geostrophic approximation. Specifically, no assumption will be made about the relative time scales associated with the deformation flow and the ageostrophic response, making the generalized model directly applicable to small, rapidly developing fronts. The

generalized model will further extend the work of HB72 by allowing wave generation and propagation, and permitting balanced and unbalanced initial conditions.

Here, as in B00 and HB72, our focus is on the early stages of frontogenesis. As such, we will follow previous studies in making two major simplifications. First, we will consider inviscid quasi-two-dimensional flow between rigid horizontal surfaces, neglecting variations in the along-front direction. Second, we will neglect the explicit nonlinear terms appearing in the equations written in momentum coordinates. We emphasize that the equations still include nonlinear effects via the use of momentum coordinates; specifically, the nonlinear cross-front advection that is responsible for rapid frontal sharpening. The neglect of nonlinear terms is also consistent with previous studies (e.g. B00 and HB72), and the validity of the approximation will be assessed in the [Appendix](#). Both of these simplifying assumptions limit the ability of the generalized model to describe the late stages of frontogenesis and frontal arrest. Nevertheless, we anticipate that the model framework will be useful in describing frontogenesis under a wide range of conditions, and providing a framework to identify three-dimensional instabilities that arise during the later stages of frontal development, which will be the subject of a future study.

The paper will be organized as follows. The basic equations and the new coordinate system will be introduced in §2 and the problem reduced to a simplified set of governing equations in §2.1. These simplified equations will be applied in §3 to derive the generalized zero PV solution, and in §4 to determine the uniform PV mass imbalance solution. The physical behaviour of the uniform PV solution will be investigated for both the frontogenetic case (i.e. where a frontal discontinuity forms) and the non-frontogenetic case, where the system undergoes geostrophic adjustment to a steady state. In §4.2 we derive the uniform PV solution of HB72 as a late-time and small-strain limit of the general solution. Furthermore, we demonstrate that the full solution for *weakly* strain-forced frontogenesis in non-zero uniform PV flow is composed of a time-varying mean state given by the HB72 solution, plus an inertia–gravity wave field, and we describe the dynamics of these waves. Lastly, in §5 we make some final remarks on the practicality of employing the framework developed herein to study the breakdown of fronts.

2. The model

We begin with the incompressible, inviscid, hydrostatic, Boussinesq equations for a rotating fluid in Cartesian coordinates. Here, we will use (U, V, W) to denote the velocity components in the (x, y, z) directions, respectively, P the pressure, ρ_0 the reference density, b the buoyancy and f the (constant) Coriolis parameter. Following HB72, a balanced (but not necessarily low-Rossby-number) large-scale deformation field of $\bar{U} = -\alpha x$ and $\bar{V} = \alpha y$ is introduced and we restrict our analysis to the case where the strain α is constant. The velocity and pressure fields may be written as

$$U = \bar{U} + u(x, z, t), \quad (2.1a)$$

$$V = \bar{V} + v(x, z, t), \quad (2.1b)$$

$$W = w(x, z, t), \quad (2.1c)$$

$$P = \bar{P} + p(x, z, t), \quad (2.1d)$$

where the perturbation fields (denoted by lower-case symbols) are explicitly assumed to be independent of y , which will be approximately true for any sufficiently long front oriented along the y -axis. The mean pressure field is $\bar{P}/\rho_0 = -\alpha^2(x^2 + y^2)/2 +$

$f\alpha xy$. Upon substitution of (2.1), the governing equations for the two-dimensional perturbation fields become

$$\frac{Du}{Dt} - fv = \alpha u - \frac{1}{\rho_0} \frac{\partial p}{\partial x}, \quad (2.2a)$$

$$\frac{Dv}{Dt} + fu = -\alpha v, \quad (2.2b)$$

$$0 = b - \frac{1}{\rho_0} \frac{\partial p}{\partial z}, \quad (2.2c)$$

$$\frac{Db}{Dt} = 0, \quad (2.2d)$$

$$\frac{\partial u}{\partial x} + \frac{\partial w}{\partial z} = 0, \quad (2.2e)$$

with the material derivative defined as

$$\frac{D}{Dt} \equiv \frac{\partial}{\partial t} + (u + \bar{U}) \frac{\partial}{\partial x} + w \frac{\partial}{\partial z}. \quad (2.3)$$

The only change from the standard two-dimensional hydrostatic rotating fluid equations (e.g. B00, (1)–(5)) is the addition of the forcing terms from the deformation field in the horizontal momentum equations. For convenience, we write the pressure field in terms of a geostrophic velocity,

$$v_g = \frac{1}{\rho_0 f} \frac{\partial p}{\partial x}, \quad (2.4)$$

and relate it to the buoyancy field b using (2.2c),

$$\frac{\partial v_g}{\partial z} = \frac{1}{f} \frac{\partial b}{\partial x}. \quad (2.5)$$

Equation (2.5) is the usual thermal wind relation. With the above definitions the horizontal momentum equations from (2.2) become

$$\frac{Du}{Dt} = f(v - v_g) + \alpha u, \quad (2.6a)$$

$$\frac{Dv}{Dt} = -fu - \alpha v. \quad (2.6b)$$

To study frontogenesis in a general framework we introduce a new coordinate system defined by

$$X = e^{\alpha t} \left(x + \frac{v}{f} \right), \quad Z = z, \quad T = t. \quad (2.7)$$

These coordinates reduce to the ‘momentum coordinates’ of B00 when $\alpha = 0$ and the ‘geostrophic coordinates’ employed by HB72 when $\exp(\alpha t)$ is set to 1 and the along-front velocity v is replaced by the geostrophic velocity v_g . Note that in the B00 case the X coordinate is conserved (and hence the absolute momentum $\mathcal{M} = fx + v$ is also conserved – hence the name *momentum* coordinates) while in the HB72 case the X coordinate is not conserved. The key feature of the new coordinates (2.7) is that the X coordinate is conserved for any value of α , and hence we will refer to (2.7) as ‘generalized momentum coordinates’. In this coordinate system, the material derivative

reduces to

$$\frac{D}{Dt} = \frac{\partial}{\partial T} + w \frac{\partial}{\partial Z}, \tag{2.8}$$

which greatly simplifies the analysis. Employing these coordinates allows us to simultaneously study the mass imbalance frontogenesis problem of B00 and the deformation frontogenesis problem of HB72 – but without the latter’s assumption of semigeostrophy. The partial derivatives and Jacobian of the coordinate transformation, and the potential vorticity and volume conservation equations in coordinates (2.7), are given in table 1. Applying these derivatives, the thermal wind relation (2.5) expressed in generalized momentum coordinates is

$$e^{-\alpha T} \frac{\partial v_g}{\partial Z} - \frac{1}{f} \frac{\partial b}{\partial X} = \frac{1}{f} \left(\frac{\partial v}{\partial X} \frac{\partial v_g}{\partial Z} - \frac{\partial v}{\partial Z} \frac{\partial v_g}{\partial X} \right). \tag{2.9}$$

The cross-derivative term on the right-hand side of this expression has been neglected in previous papers employing momentum coordinates (e.g. (3.3) of Blumen & Williams 2001). The term does vanish exactly in the special case where the full along-front velocity is related to the geostrophic velocity through multiplication by a function h dependent only on time T ,

$$v(X, Z, T) = h(T) v_g(X, Z, T). \tag{2.10}$$

In the case of the semigeostrophic HB72 model, $v \equiv v_g$ or $h(T) = 1$, and hence the cross-derivative term of (2.9) does indeed vanish. Similarly, at steady state $v = v_g$ and hence the right-hand side of (2.9) vanishes. (This result was used by Blumen & Wu (1995) and Wu & Blumen (1995): see their equations (10) and (3), respectively.) The B00 solution also takes the form of (2.10), although no assumption to this effect was made *a priori*. In general, however, the nonlinear term in (2.9) will not vanish identically. To aid in later analysis we write the thermal wind as the linear solution to (2.9), plus a nonlinear correction Δv_g ,

$$v_g = \frac{1}{f} e^{\alpha T} \int \frac{\partial b}{\partial X} dZ + \Delta v_g, \tag{2.11}$$

where the correction is given by the exact thermal wind (as defined in Eulerian coordinates) minus the approximate solution (evaluated in momentum coordinates),

$$\Delta v_g = \frac{1}{f} \int \frac{\partial b}{\partial x} dz - \frac{1}{f} e^{\alpha T} \int \frac{\partial b}{\partial X} dZ. \tag{2.12}$$

Before proceeding with the model, it is useful to introduce appropriate non-dimensional parameters. The relevant physical variables are the inertial frequency f , horizontal buoyancy gradient M^2 , buoyancy frequency N , strain α , horizontal (x) length scale L , and height scale H . The buoyancy scale is taken to be $b \sim M^2 L$ and time scaled inertially $T \sim 1/f$, leading to a horizontal velocity scale of $U \sim \sqrt{bH} = \sqrt{M^2 LH}$ and a vertical velocity scale of $W \sim UH/L = \sqrt{M^2 H^3/L}$ from continuity equation (2.2e). There are three independent non-dimensional parameters in the hydrostatic limit which we choose as the Rossby number,

$$Ro = \frac{U}{fL} = \sqrt{\frac{M^2 H}{f^2 L}}, \tag{2.13}$$

	Symbol	Dimensional	Non-dimensional
x coordinate	X	$e^{\alpha T} \left(x + \frac{v}{f} \right)$	$e^{\delta T} (x + Ro v)$
Jacobian	J	$e^{\alpha T} \left(1 - e^{\alpha T} \frac{1}{f} \frac{\partial v}{\partial X} \right)^{-1}$	$e^{\delta T} \left(1 - e^{\delta T} Ro \frac{\partial v}{\partial X} \right)^{-1}$
t derivative	$\frac{\partial}{\partial t}$	$\frac{\partial}{\partial T} + \left(\alpha X e^{-\alpha T} + \frac{1}{f} \frac{\partial v}{\partial T} \right) J \frac{\partial}{\partial X}$	$\frac{\partial}{\partial T} + \left(\delta X e^{-\delta T} + Ro \frac{\partial v}{\partial T} \right) J \frac{\partial}{\partial X}$
x derivative	$\frac{\partial}{\partial x}$	$J \frac{\partial}{\partial X}$	$J \frac{\partial}{\partial X}$
z derivative	$\frac{\partial}{\partial z}$	$\frac{\partial}{\partial Z} + \frac{1}{f} \frac{\partial v}{\partial Z} J \frac{\partial}{\partial X}$	$\frac{\partial}{\partial Z} + Ro \frac{\partial v}{\partial Z} J \frac{\partial}{\partial X}$
Potential vorticity	q	$\frac{\partial b}{\partial Z} \left(1 - e^{\alpha T} \frac{1}{f} \frac{\partial v}{\partial X} \right)^{-1}$	$\frac{\partial b}{\partial Z} \left(1 - e^{\delta T} Ro \frac{\partial v}{\partial X} \right)^{-1}$
Effective u	u_*	$u + \frac{w}{f} \frac{\partial v}{\partial Z}$	$u + Ro w \frac{\partial v}{\partial Z}$
Effective w	w_*	$w J^{-1}$	$w J^{-1}$
Continuity equation		$\frac{\partial u_*}{\partial X} + \frac{\partial w_*}{\partial Z} = 0$	$\frac{\partial u_*}{\partial X} + \frac{\partial w_*}{\partial Z} = 0$

TABLE 1. Quantities of interest expressed in generalized momentum coordinates in both dimensional and non-dimensional forms. The effective velocities were defined by Blumen (2000) and have been generalized here to include the deformation field. The definition of the potential vorticity is taken as $q = (\mathbf{k} + f^{-1} \nabla \times \mathbf{U}) \cdot \nabla b$ where \mathbf{k} is a unit vector in the z -direction.

Froude number,

$$F = \sqrt{\frac{(U/H)^2}{N^2}} = \sqrt{\frac{M^2 L}{N^2 H}}, \quad (2.14)$$

and deformation ratio,

$$\delta = \frac{\alpha}{f}. \quad (2.15)$$

The deformation ratio may also be interpreted as the Rossby number pertaining to the large-scale cross-front strain flow; that is, $\delta = \bar{U}/(fL) = (\alpha L)/(fL) = \alpha/f$. Another dependent non-dimensional number that will prove useful is the Burger number,

$$Bu = \frac{Ro}{F} = \frac{NH}{fL}. \quad (2.16)$$

Equations (2.6) can now be rewritten in non-dimensional form (henceforth non-dimensional form should be assumed unless otherwise noted) as

$$\frac{Du}{Dt} = (v - v_g) + \delta u, \quad (2.17a)$$

$$\frac{Dv}{Dt} = -u - \delta v, \quad (2.17b)$$

with the non-dimensional material derivative in generalized momentum coordinates defined by

$$\frac{D}{Dt} = \frac{\partial}{\partial T} + Ro w \frac{\partial}{\partial Z}. \quad (2.18)$$

The non-dimensional thermal wind relation (from (2.9)) is

$$e^{-\delta T} \frac{\partial v_g}{\partial Z} - Ro \frac{\partial b}{\partial X} = Ro \left(\frac{\partial v}{\partial X} \frac{\partial v_g}{\partial Z} - \frac{\partial v}{\partial Z} \frac{\partial v_g}{\partial X} \right). \quad (2.19)$$

The non-dimensional expressions for PV conservation and other quantities of interest are shown alongside their dimensional forms in table 1. The non-dimensional parameters and variables are summarized in table 2.

Equations (2.17) comprise a set of two first-order differential equations (in the material derivative) which may be reduced to a single second-order equation by eliminating u :

$$\frac{D^2 v}{Dt^2} + (1 - \delta^2) v = v_g. \quad (2.20)$$

The double material derivative in (2.20) may be expanded as

$$\frac{D^2 v}{Dt^2} = \frac{\partial^2 v}{\partial T^2} + \left(2Ro w \frac{\partial^2 v}{\partial Z \partial T} + Ro^2 w^2 \frac{\partial^2 v}{\partial Z^2} + Ro \frac{Dw}{Dt} \frac{\partial v}{\partial Z} \right) = \frac{\partial^2 v}{\partial T^2} + \mathcal{N}, \quad (2.21)$$

where \mathcal{N} represents the nonlinear terms (which correspond to the vertical advection of horizontal momentum along lines of constant momentum X). The full set of non-dimensional equations describing the system is given by (2.20), together with the

Buoyancy scale		$M^2 L$
Horizontal velocity scale		$\sqrt{M^2 L H}$
Vertical velocity scale		$\sqrt{\frac{M^2 H^3}{L}}$
Time scale		$\frac{1}{f}$
Rosby number	Ro	$\sqrt{\frac{M^2 H}{f^2 L}}$
Froude number	F	$\sqrt{\frac{M^2 L}{N^2 H}}$
Deformation ratio	δ	$\frac{\alpha}{f}$
Burger number (Ro/F)	Bu	$\frac{NH}{fL}$
Geostrophic Rossby number	Ro_g	Ro^2
Geostrophic Froude number	F_g	$Ro F$

TABLE 2. Non-dimensional parameters and variable scales employed herein. The fundamental physical scales are the inertial frequency f , horizontal buoyancy gradient M^2 , buoyancy frequency N , strain α , horizontal length L , and height H . The geostrophic Rossby and Froude numbers, defined in terms of the geostrophic velocity scale $U_g \sim M^2 H/f$, are also shown to assist in comparison of the present work with other studies.

thermal wind relation (2.19), buoyancy conservation (2.2d), and PV conservation,

$$\frac{Dq}{Dt} = 0, \quad (2.22)$$

where the PV, q , is given in table 1.

2.1. The general solution for uniform PV flow

The two-dimensional geostrophic adjustment and frontogenesis problem (e.g. Rossby 1938; Hoskins & Bretherton 1972; Wu & Blumen 1995; Blumen 2000) involves analysing the response to an initial mass imbalance (an unbalanced buoyancy gradient in the x direction) or momentum imbalance (an unbalanced horizontal flow). Since one of our primary objectives is to extend the analysis of B00 to include a deformation field, we will primarily focus on the mass imbalance problem with an initial condition of no motion, the same initial condition as in B00. Following previous authors, we consider a flow that is unbounded in the X direction and trapped between rigid lids (i.e. $w = 0$) at $Z = 0$ and $Z = 1$.

We suppose that the PV, as defined in table 1, is initially uniform and without loss of generality define the buoyancy field as

$$b(X, Z, T) = b_0(X) + F^{-2} Z + \Delta b(X, Z, T). \quad (2.23)$$

In B00 the field $b_0(X)$ constitutes the initial imposed mass imbalance to which the system must adjust, while in HB72 the field $b_0(X)$ corresponds to the imposed surface ($Z = 0, 1$) distribution of buoyancy. Consistent with both these interpretations, we require that the buoyancy anomaly Δb vanishes on the rigid lid boundaries at time zero. Applying buoyancy conservation (2.2d) on the boundaries we obtain

$$\left. \frac{Db}{Dt} \right|_{Z=0,1} = \left. \frac{\partial b}{\partial T} \right|_{Z=0,1} = \left. \frac{\partial \Delta b}{\partial T} \right|_{Z=0,1} = 0, \quad (2.24)$$

and thus the buoyancy anomaly remains identically zero on the boundaries for all time. In the case where the buoyancy anomaly Δb is initially everywhere zero, the system is completely unbalanced at time zero (as in the B00 model). We can also consider cases where Δb is non-zero in the interior in the initial state and the system is therefore balanced (or partially balanced) at time zero (as in the HB72 model), as long as the constraint of uniform potential vorticity holds for the initial state.

In light of PV conservation, the PV will remain uniform for all time, and upon substitution of the functional form of the buoyancy (2.23), PV conservation (2.22) reduces to

$$\frac{\partial \Delta b}{\partial Z} = -Ro F^{-2} e^{\delta T} \frac{\partial v}{\partial X}, \quad (2.25)$$

where we have required that the buoyancy anomaly and velocity field vanish as $X \rightarrow \pm\infty$ and hence $q \equiv F^{-2}$. The buoyancy anomaly field may thus be uniquely determined from knowledge of the along-front velocity $v(X, Z, T)$ by integration of (2.25) and application of the boundary condition (2.24):

$$\Delta b(X, Z, T) = -Ro F^{-2} e^{\delta T} \int_0^Z \frac{\partial v}{\partial X} dZ'. \quad (2.26)$$

The total buoyancy field (in terms of v) is obtained by substitution of the anomaly (2.26) into (2.23):

$$b(X, Z, T) = b_0(X) + F^{-2} Z - Ro F^{-2} e^{\delta T} \int_0^Z \frac{\partial v}{\partial X} dZ'. \quad (2.27)$$

Next, we substitute the buoyancy (2.27) into the buoyancy conservation equation (2.2d) to yield an expression for the vertical velocity,

$$\frac{Db}{Dt} = 0 \Rightarrow w = \frac{D}{Dt} \left(e^{\delta T} \int_0^Z \frac{\partial v}{\partial X} dZ' \right). \quad (2.28)$$

Expanding the total derivative on the right-hand side, we obtain an expression for an effective vertical velocity w_* (as listed in table 1),

$$w_* = w J^{-1} = w \left(1 - Ro e^{\delta T} \frac{\partial v}{\partial X} \right) e^{-\delta T} = e^{-\delta T} \int_0^Z \frac{\partial}{\partial T} \left(e^{\delta T} \frac{\partial v}{\partial X} \right) dZ', \quad (2.29)$$

from which the actual vertical velocity w may be readily obtained. This is a very useful expression. For example, (2.29) generates the vertical velocity field for both the B00 and HB72 models from their specified along-front velocity fields. Also, using

(2.29), the cross-front streamfunction may be derived as

$$\begin{aligned}\psi &= -\int w dx = -\int_{-\infty}^X w J^{-1} dX' = -\int_{-\infty}^X \int_0^Z \frac{\partial}{\partial T} \left(e^{\delta T} \frac{\partial v}{\partial X'} \right) e^{-\delta T} dZ' dX' \\ &= -e^{-\delta T} \frac{\partial}{\partial T} \left(e^{\delta T} \int_0^Z v dZ' \right),\end{aligned}\quad (2.30)$$

by substitution of the Jacobian from table 1 and assuming that v vanishes far from the front, at $X = -\infty$. Equation (2.30) implies that if the along-front flow $v(X, Z, T)$ is known for any two-dimensional uniform PV fluid subject to a strain α , then the flow in the cross-front plane can be found. The cross-front velocity u may be expressed using (2.30) as

$$\begin{aligned}u &= \frac{\partial \psi}{\partial z} = \frac{\partial \psi}{\partial Z} + Ro \frac{\partial v}{\partial Z} J \frac{\partial \psi}{\partial X} \\ &= -\frac{\partial v}{\partial T} - \delta v - Ro w \frac{\partial v}{\partial Z}\end{aligned}\quad (2.31)$$

$$= -\frac{Dv}{Dt} - \delta v \quad (2.32)$$

by substitution of the appropriate derivatives from table 1. Note that (2.32) is merely a restatement of the non-dimensional y -momentum equation (2.17b). It will prove useful to rewrite (2.31) in terms of an effective velocity u_* (listed in table 1) as

$$u_* = u + Ro w \frac{\partial v}{\partial Z} = -\frac{\partial v}{\partial T} - \delta v. \quad (2.33)$$

Since the cross-front flow, u and w , can be written in terms of the along-front velocity, v , all that remains is to solve for the along-front jet $v(X, Z, T)$. An exact, albeit symbolic, expression may be obtained via substitution of the geostrophic velocity v_g from (2.11) and the buoyancy field from (2.27) into the combined horizontal momentum equation (2.20),

$$\begin{aligned}\frac{\partial^2 v}{\partial T^2} + (1 - \delta^2) v + Bu^2 e^{2\delta T} \int \int_0^Z \frac{\partial^2 v}{\partial X^2} dZ' dZ - Ro e^{\delta T} b'_0(X) \left(Z - \frac{1}{2} \right) \\ = \Delta v_g - \mathcal{N},\end{aligned}\quad (2.34)$$

where there is a constant of integration $C(X, T)$ associated with the indefinite integral. To remove this unknown constant we subtract the vertical average of (2.34) from (2.34) to form an equation in the baroclinic velocity v^* ,

$$\begin{aligned}\frac{\partial^2 v^*}{\partial T^2} + (1 - \delta^2) v^* + Bu^2 e^{2\delta T} \int^* \int_0^Z \frac{\partial^2 v^*}{\partial X^2} dZ' dZ - Ro e^{\delta T} b'_0(X) \left(Z - \frac{1}{2} \right) \\ = \Delta v_g^* - \mathcal{N}^*,\end{aligned}\quad (2.35)$$

where superscript $*$ denotes the baroclinic part of the integral. The barotropic part of the along-front flow, \bar{v} , may be determined by vertically averaging the continuity equation (from table 1) in momentum coordinates, to obtain

$$\frac{\partial \bar{u}_*}{\partial X} = 0 \Rightarrow \bar{u}_* = \bar{u}_*(T), \quad (2.36)$$

and since \bar{u}_* , as defined by (2.33), must vanish far from the front, $\bar{u}_* = 0$. Thus, vertically averaging (2.33) we obtain

$$\bar{u}_* = -\frac{\partial \bar{v}}{\partial T} - \delta \bar{v} = 0 \Rightarrow \bar{v} = e^{-\delta T} v_0(X). \quad (2.37)$$

The velocity $v_0(X)$ is known as the barotropic jet (see e.g. Wu & Blumen 1995; Plougonven & Zeitlin 2005) and is set by the choice of initial conditions – we set $v_0(X) = 0$ herein. With this choice, (2.35) describes the time evolution of the full along-front velocity field, $v \equiv v^*$. All nonlinear terms have been placed on the right-hand side of (2.35). Recall that Δv_g^* (2.12) corresponds to nonlinear effects arising from the thermal wind equation, and \mathcal{N}^* (2.21) to nonlinear vertical advection. We expect that these nonlinear terms will be second-order for an appropriate choice of initial conditions, except in the limit of discontinuity formation, and thus neglect the right-hand side of (2.35) to obtain

$$\frac{\partial^2 v}{\partial T^2} + (1 - \delta^2) v + Bu^2 e^{2\delta T} \int_0^* \int_0^Z \frac{\partial^2 v}{\partial X^2} dZ' dZ = Ro e^{\delta T} b'_0(X) \left(Z - \frac{1}{2} \right). \quad (2.38)$$

The neglect of the nonlinear terms is justified *a posteriori* in the Appendix by direct computation of the two nonlinear terms, Δv_g^* and $-\mathcal{N}^*$, from the linearized solutions. We find that where the linearized solution predicts the occurrence of a discontinuity, the nonlinear terms do indeed remain second-order until near this time, and only become large in the vicinity of the discontinuity. In cases where a discontinuity is not predicted, the nonlinear terms remain second-order for all time, and trend to zero as the system approaches a steady state. Furthermore, (2.38) produces solutions consistent with previous nonlinear studies such as B00 and HB72. For example, B00 explicitly assume the nonlinear advection terms to vanish (see his equation (20)) and HB72 implicitly neglect the terms through the assumption of semigeostrophy and thus the neglect of the cross-front acceleration Du/Dt .

Equation (2.38), together with the cross-front circulation (2.29), (2.30) and (2.33) and buoyancy anomaly (2.26), will form the basis for most of our subsequent analysis. Equation (2.38) may also be usefully rewritten in terms of the buoyancy anomaly by taking derivatives with respect to X and Z and substituting for v using (2.26):

$$\left[\frac{\partial^2}{\partial Z^2} \left(\frac{\partial^2}{\partial T^2} - 2\delta \frac{\partial}{\partial T} + 1 \right) + Bu^2 e^{2\delta T} \frac{\partial^2}{\partial X^2} \right] \Delta b = -Bu^2 e^{2\delta T} b''_0(X). \quad (2.39)$$

The relevant boundary conditions are that Δb vanish at the rigid lids, $Z = 0, 1$, and far from the front, $X \rightarrow \pm\infty$.

Before analysing fully time-dependent frontogenesis, it is worth examining our solution in the semigeostrophic limit ($v \simeq v_g$) to demonstrate consistency with the work of previous authors (e.g. Eliassen 1962; Hoskins & Bretherton 1972; Davies & Muller 1988; Blumen & Wu 1995, etc.). Referring to the combined momentum equation (2.20), the limit $v \simeq v_g$ requires that

$$\frac{D^2 v}{Dt^2}, \quad \delta^2 v \ll v, \quad (2.40)$$

or equivalently that the strain δ is small and time derivatives are negligible. Applying these approximations to (2.39), one obtains a form of Laplace's equation:

$$\left(\frac{\partial^2}{\partial Z^2} + Bu^2 e^{2\delta T} \frac{\partial^2}{\partial X^2} \right) (b_0(X) + \Delta b) = 0. \quad (2.41)$$

A similar equation to (2.41) appears in HB72 (equation (3.47)), Blumen & Wu (1995, equation (26)) and Plougonven & Zeitlin (2005, equation (33)). Furthermore, one may write the buoyancy anomaly (2.26) in terms of the streamfunction (2.30),

$$\Delta b = Ro F^{-2} \int_0^T e^{\delta T'} \frac{\partial \psi}{\partial X} dT', \quad (2.42)$$

which, upon substitution into Laplace's equation (2.41) and some further algebra, yields the generalized momentum coordinate formulation of the semigeostrophic Sawyer–Eliassen equation for uniform PV flow (e.g. compare with Davies & Muller 1988, equation (17)),

$$Bu^2 e^{2\delta T} \frac{\partial^2 \psi}{\partial X^2} + \frac{\partial^2 \psi}{\partial Z^2} = -2\delta Ro e^{\delta T} \frac{\partial b}{\partial X}. \quad (2.43)$$

The right-hand side of (2.43) constitutes the frontogenetic forcing of the ageostrophic flow by the large-scale strain field. The solution to either (2.41) or (2.43) yields the uniform PV deformation frontogenesis solution of HB72 for $\delta \neq 0$, and the steady state solution to the mass imbalance problem obtained by Blumen & Wu (1995) when $\delta = 0$. Hence, as noted by Plougonven & Zeitlin (2005), the HB72 deformation problem may be considered as a succession of geostrophic adjustments to a steady state neglecting the oscillatory behaviour of (2.38).

3. Inertial oscillations and frontogenesis in zero PV flow

Equation (2.38) provides a unified framework for analysing frontogenesis and geostrophic adjustment in a two-dimensional flow of uniform (but arbitrary) potential vorticity. Before considering the system more generally, it is enlightening to discuss the special case of zero potential vorticity, which corresponds to vanishingly small background stratification N and Burger number Bu . In addition to being more tractable analytically, this special subset of uniform PV flows is commonly studied in its own right since the boundary layers where fronts form in the atmosphere and ocean often have very weak stratification. For example, an estimate of the Burger number in the ocean mixed layer, using typical values (see e.g. Boccaletti, Ferrari & Fox-Kemper 2007) of $N \sim 10^{-3} \text{ s}^{-1}$, $f \sim 10^{-4} \text{ s}^{-1}$ and aspect ratio $L/H \sim 100$, yields $Bu = NH/(fL) = 10^{-1}$. The neglect of the term involving the Burger number in the governing differential equation (2.38) will therefore introduce an error of only $\sim 1\%$ in this situation, and hence the zero PV model is a very good approximation.

Setting the Burger number to zero, (2.38) becomes simply

$$\frac{\partial^2 v}{\partial T^2} + (1 - \delta^2) v = e^{\delta T} Ro b'_0(X) \left(Z - \frac{1}{2} \right), \quad (3.1)$$

subject to appropriate initial conditions. Here we will consider initial conditions of zero anomalous motion in the cross-front plane, $u = w = 0$, and an along-front velocity of

$$v = (1 - \epsilon) v_g, \quad (3.2)$$

where $0 \leq \epsilon \leq 1$. The imbalance fraction ϵ allows us to control the degree of initial imbalance: if $\epsilon = 0$ the system begins in its geostrophically adjusted state and there is no mass imbalance, while for greater ϵ there exists an initial thermal wind that *partially* balances the imposed horizontal buoyancy gradient. The initial conditions match those of B00 when $\epsilon = 1$, corresponding to no initial motion and a fully

unbalanced initial state. The initial conditions do not match those of HB72: the initial conditions in that model are implied by the assumption of (semigeostrophic) balance. One of the limitations of the HB72 model is that the initial conditions in a given geophysical context are unlikely to be in exact semigeostrophic balance. We examine the case of geostrophic balance ($v = v_g$) but semigeostrophic imbalance ($u = w = 0$) as a convenient set of initial conditions to investigate the presence of inertial oscillations in the solution. Such oscillations appear to be a common feature of frontal systems (e.g. Snyder, Skamarock & Rotunno 1993; Ostdiek & Blumen 1997).

Substitution of the initial conditions $u = w = 0$ into the expression for u (2.31) results in a second initial condition on v of

$$\frac{\partial v}{\partial T} + \delta v = 0. \tag{3.3}$$

Solving (3.1) with initial conditions (3.2) and (3.3) yields

$$v = Ro b'_0(X) \left(Z - \frac{1}{2} \right) \left(e^{\delta T} - \epsilon \cos \sqrt{1 - \delta^2} T + \frac{\delta(\epsilon - 2)}{\sqrt{1 - \delta^2}} \sin \sqrt{1 - \delta^2} T \right). \tag{3.4a}$$

The cross-front velocity may now be generated from (2.31) as

$$u = -Ro b'_0(X) \left(Z - \frac{1}{2} \right) \left(2\delta (e^{\delta T} - \cos \sqrt{1 - \delta^2} T) + \frac{\epsilon - 2\delta^2}{\sqrt{1 - \delta^2}} \sin \sqrt{1 - \delta^2} T \right) - Ro w \frac{\partial v}{\partial Z}, \tag{3.4b}$$

and the vertical velocity from (2.29) as

$$w = \frac{Ro b''_0(X) Z(Z - 1) e^{\delta T} \left(\delta (e^{\delta T} - \cos \sqrt{1 - \delta^2} T) + \frac{\epsilon - 2\delta^2}{2\sqrt{1 - \delta^2}} \sin \sqrt{1 - \delta^2} T \right)}{1 - Ro e^{\delta T} \frac{\partial v}{\partial X}}. \tag{3.4c}$$

The general solution (3.4) depends on only two non-dimensional parameters: Ro and δ . The solution is composed of (i) an exponential growth driven by the large-scale strain field, and (ii) near-inertial (presuming $\delta \ll 1$) oscillations resulting from both the initial conditions (with relative amplitude ϵ) and the deformation forcing (with relative amplitude δ). Previous solutions have either considered the exponentially growing part (e.g. HB72, balanced) or the oscillatory part (e.g. B00, unbalanced) in isolation. However, the two effects are known to occur simultaneously. For example, in Ostdiek & Blumen (1997) observations pertaining to the movement of an atmospheric front over the central USA are described and compared with HB72 theory. A significant feature of the observed wind fields in the frontal zone is the presence of strong inertial oscillations that cause a departure from the HB72 prediction (see also Blumen 1997).

The zero PV solutions of HB72 and B00 may now be obtained as limits of the general solution given above. Setting the initial imbalance to zero ($\epsilon = 0$) yields a modified version of the HB72 solution that satisfies the condition of no flow in the x and z directions at time zero. If we additionally suppose that $T \gg 1$ such that the oscillations are negligible in comparison to the directly forced part of the flow, we

recover the exact HB72 solution in non-dimensional form:

$$u = -e^{\delta T} Ro b'_0(X) (Ro w + (2Z - 1) \delta), \quad (3.5a)$$

$$v = v_g = e^{\delta T} Ro b'_0(X) \left(Z - \frac{1}{2} \right), \quad (3.5b)$$

$$w = Ro \delta b''_0(X) Z(Z - 1) e^{2\delta T} \left(1 - Ro e^{\delta T} \frac{\partial v}{\partial X} \right)^{-1}. \quad (3.5c)$$

We emphasize that this HB72 solution is in general only valid at times of $O(\alpha^{-1})$, where α is the dimensional strain. In particular, the neglect of the initial conditions (and their corresponding oscillations) in this HB72 solution places a constraint on the size of the Rossby number (see below). Returning to the general solution, if we instead set $\delta = 0$ and $\epsilon = 1$, we obtain a non-dimensional version of the B00 solution:

$$u = -Ro b'_0(X) \left(\left(Z - \frac{1}{2} \right) \sin T + Ro w (1 - \cos T) \right), \quad (3.6a)$$

$$v = Ro b'_0(X) \left(Z - \frac{1}{2} \right) (1 - \cos T), \quad (3.6b)$$

$$w = \frac{1}{2} Ro b''_0(X) Z(Z - 1) \sin T \left(1 - Ro \frac{\partial v}{\partial X} \right)^{-1}. \quad (3.6c)$$

This solution (3.6) is valid for all time, with no restrictions on the size of the Rossby number.

The criterion for the formation of a frontal discontinuity is that the inverse Jacobian of the coordinate transformation (from table 1),

$$J^{-1} = e^{-\delta T} - Ro \frac{\partial v}{\partial X}, \quad (3.7)$$

vanishes. In the B00 case (3.6b) it is the initial imbalance that drives frontogenesis through the inertial oscillatory response of the system, and thus a singularity will only occur for a sufficiently large Rossby number,

$$Ro^2 \max |b''_0(X)| \geq 1. \quad (3.8)$$

The *critical* Rossby number is the minimum value required for a singularity to occur,

$$Ro_c = \frac{1}{\sqrt{\max |b''_0(X)|}}, \quad (3.9)$$

and is $O(1)$, although the exact value depends on the initial profile $b_0(X)$. In this case frontogenesis occurs on an *inertial* time scale f^{-1} with the dimensional critical time, t_c (i.e. the time taken for a singularity to form) given by

$$ft_c = \arccos \left(1 - 2 \left(\frac{Ro_c}{Ro} \right)^2 \right). \quad (3.10)$$

In contrast, in the HB72 case the along-front velocity (3.5b) grows exponentially in time, and thus any arbitrarily weak buoyancy gradient is squeezed into a front by the large-scale convergent field. In this case frontogenesis occurs on the (much longer)

	Symbol	Spontaneous (B00)	Forced (HB72)
Critical Ro	Ro_c	$\frac{1}{\sqrt{\gamma}}$	Always frontogenic
Position (GMC)	X_f	$b_0'''(X_f) = 0$	$b_0'''(X_f) = 0$
Critical time	t_c	$\frac{1}{f} \arccos\left(1 - \frac{2}{Ro^2 \gamma}\right)$	$\frac{1}{2\alpha} \ln\left(\frac{2}{Ro^2 \gamma}\right)$
Max jet velocity	v_f	$-\frac{b_0'(X_f)}{Ro \gamma}$	$-\frac{b_0'(X_f)}{\sqrt{2\gamma}}$
Position (Euler)	x_f	$X_f + \frac{b_0'(X_f)}{\gamma}$	$Ro \frac{1}{\sqrt{2\gamma}} (X_f \gamma + b_0'(X_f))$

TABLE 3. Comparison of forced and spontaneous singularity formation on the lower boundary from the B00 and HB72 models of frontogenesis, where $\gamma = -b_0''(X_f) > 0$. Note that the maximum jet velocity scales inversely with Ro in the B00 model, and is independent of Ro in the HB72 model. In contrast, the Eulerian frontal position is independent of Ro in the B00 model, and proportional to Ro in the HB72 model. The Eulerian (real space) position of frontogenesis on the lower boundary is related to the momentum coordinate (GMC) position by $x_f = \exp(-\delta t_c) X_f - Ro v_f$.

deformation field forcing time scale α^{-1} , with critical time

$$\alpha t_c = \frac{1}{2} \ln 2 - \ln\left(\frac{Ro}{Ro_c}\right). \tag{3.11}$$

As noted above, the neglect of the initial conditions in this HB72 model places a constraint on the size of the Rossby number Ro . An extreme limit is given by the values of the Rossby number, $Ro \geq \sqrt{2} Ro_c$, that make $t_c \leq 0$ in (3.11), and consequently the implied initial state invalid. The HB72 solution (for zero PV) may thus be characterized equivalently as a long-time or small-Rossby-number model of frontogenesis.

In both the B00 and HB72 cases the singularity forms at the location where $|b_0''(X)|$ is maximized. These and other characteristics of forced and spontaneous frontogenesis are listed in table 3. To visualize these results, the time evolution of the buoyancy field is shown in figure 1 for a (scaled) error function initial buoyancy profile,

$$b_0(X) = \frac{1}{2} \operatorname{erf}\left(\frac{X}{\sqrt{2}}\right), \tag{3.12}$$

having critical Rossby number $Ro_c = 2.03$, for a typical B00 imbalance case ($Ro = 3$, $\delta = 0$, $\epsilon = 1$) and a typical HB72-type forced frontogenesis case ($Ro = 0.4$, $\delta = 0.1$, $\epsilon = 0$). The isopycnal slope at time T in zero PV flow may be derived from the derivatives in table 1 as

$$\text{slope} = \frac{-\frac{\partial b}{\partial x}}{\frac{\partial b}{\partial z}} = -\frac{1}{Ro \frac{\partial v}{\partial Z}}, \tag{3.13}$$

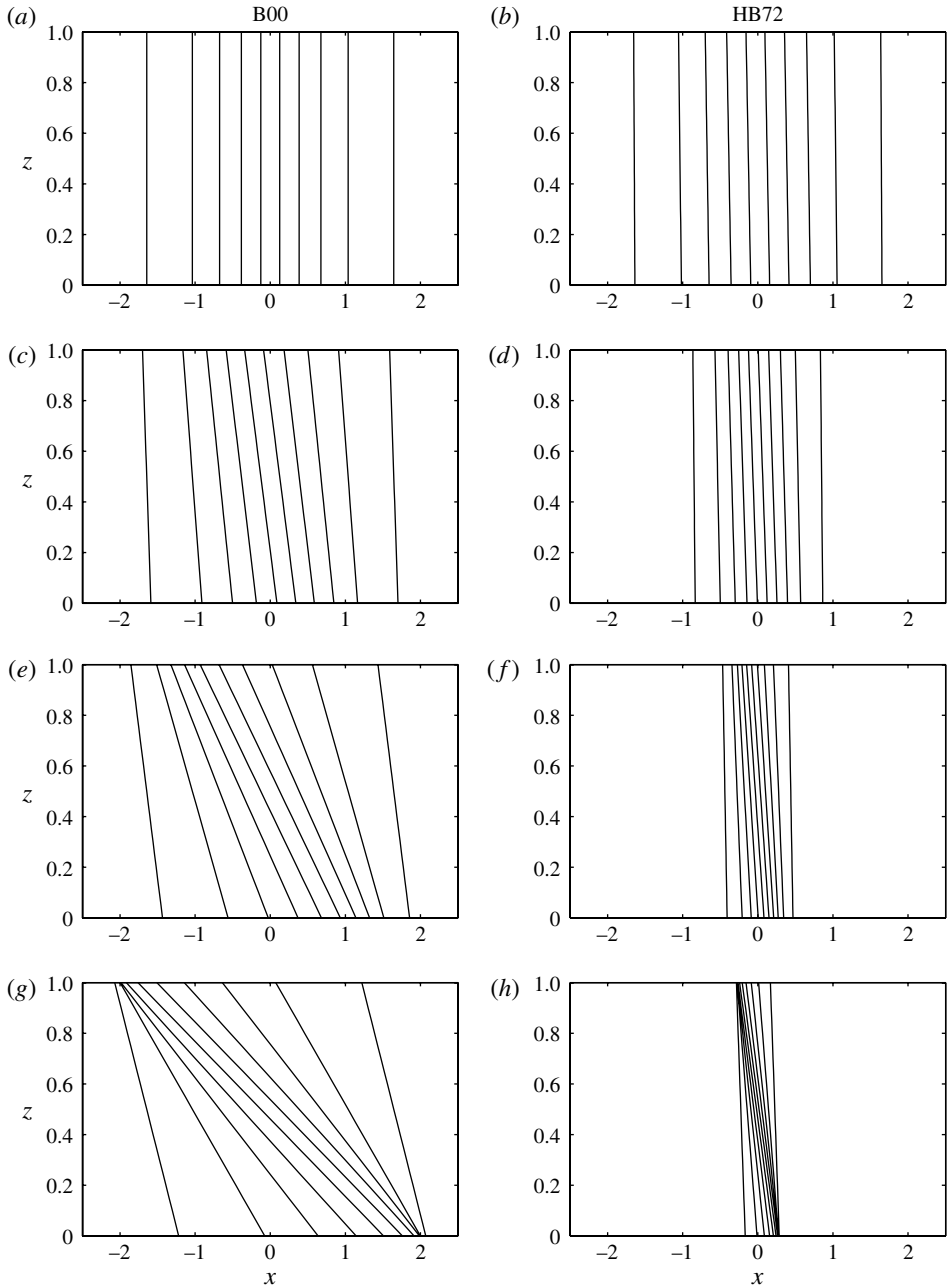


FIGURE 1. The time evolution of the buoyancy field towards frontogenesis as predicted by the general zero PV solution (3.4) for a typical B00 case ($Ro = 3$, $\delta = 0$, $\epsilon = 1$, a, c, e, g) and a typical HB72 case ($Ro = 0.4$, $\delta = 0.1$, $\epsilon = 0$, b, d, f, h) at times from top to bottom of 0 , $t_c/3$, $2t_c/3$ and t_c . The critical time is $t_c = 1.49$ in the B00 case and $t_c = 19.8$ in the HB72 case. The contour interval is 0.1 in non-dimensional units.

which is only infinite at time zero if the vertical gradient of v is zero. Hence, in the HB72 case the initial condition of geostrophic balance ($\epsilon = 0$) imposes a non-zero stratification in the imbalance region at time zero – as may be observed by the slight tilt of the isopycnals in figure 1(b). Substitution of v (3.4a) into (3.13) yields the result that the isopycnal slope is a function of only $X = X_0$ and T , and thus the isopycnals are straight lines for all time. Referring to the figure, we observe that in the B00 case the initially vertical isopycnals rapidly tilt towards the horizontal as frontogenesis proceeds. The length scale of the imbalance region remains $O(1)$ during frontogenesis, with the location of the singularity in Eulerian coordinates, x_f , defined in table 3. The location of the singularity is independent of Rossby number, and using (3.12), may be evaluated as $x_f = 2$. In contrast, in the HB72 case the large-scale convergent field squeezes the imbalance region to a length scale of $O(Ro)$ by critical time. The initially near-vertical isopycnals are tilted through a far smaller angle and therefore the isopycnal slopes at the critical time (from (3.13)) are substantially larger than in the B00 case (or equivalently the stratification is almost an order of magnitude smaller).

One major application of the general solution derived above is as a generalization of the HB72 theory that correctly accounts for arbitrary initial conditions including unbalanced flow with large Rossby numbers, thus providing a check on the applicability of the semigeostrophic approximation. With this in mind, we compare the general solution (3.4) with the semigeostrophic HB72 solution (3.5) for the specific initial buoyancy profile defined by (3.12) and parameter values of $Ro = 0.4$ and $\delta = 0.1$ (as for figure 1b,d,f,h). Figure 2 displays time series of the normalized minimum frontal width d defined similarly to Blumen & Williams (2001),

$$d = \frac{\max \left| \frac{\partial b_0}{\partial X} \right|}{\max \left| \frac{\partial b}{\partial x} \right|}, \tag{3.14}$$

and the magnitudes of the three velocity components at the position of the buoyancy gradient maximum. The solid line corresponds to the general solution with initial conditions of no motion ($\epsilon = 1$), the dotted line to the general solution with initial conditions of (baroclinic) geostrophic balance ($\epsilon = 0$), and the dashed line to the HB72 solution. The frontal width is almost indistinguishable in all three cases, implying that the HB72 prediction of the critical time (i.e. the time when d vanishes), and the buoyancy field at time T , are both accurate.

This close agreement between the models is readily explained as follows. The buoyancy field at a given time is determined from $b_0(X)$ with the momentum coordinate given by $X = x + Ro v$, and thus the difference in the buoyancy field of the HB72 solution with respect to the general solution at some x is given by

$$\Delta b \sim \frac{\partial b}{\partial X} \Delta X \sim \frac{\partial b}{\partial X} Ro (v - v_{\text{HB72}}) = \frac{\partial b}{\partial X} Ro v_a. \tag{3.15}$$

The ageostrophic velocity v_a (from (3.4a)) is at most $Ro/2$ and thus Δb is at most $Ro^2/2$. Therefore the maximum error in d and the buoyancy field for $Ro = 0.4$ is less than 10%. Referring to the figure, the agreement in the along-front velocity itself is also very strong for the initially balanced case (since $v_a \sim \delta v_g$ initially), whereas in the case of zero initial motion the oscillations in v triggered by the mass imbalance are significant ($v_a \sim v_g$ initially). More generally, the oscillation amplitude for all field

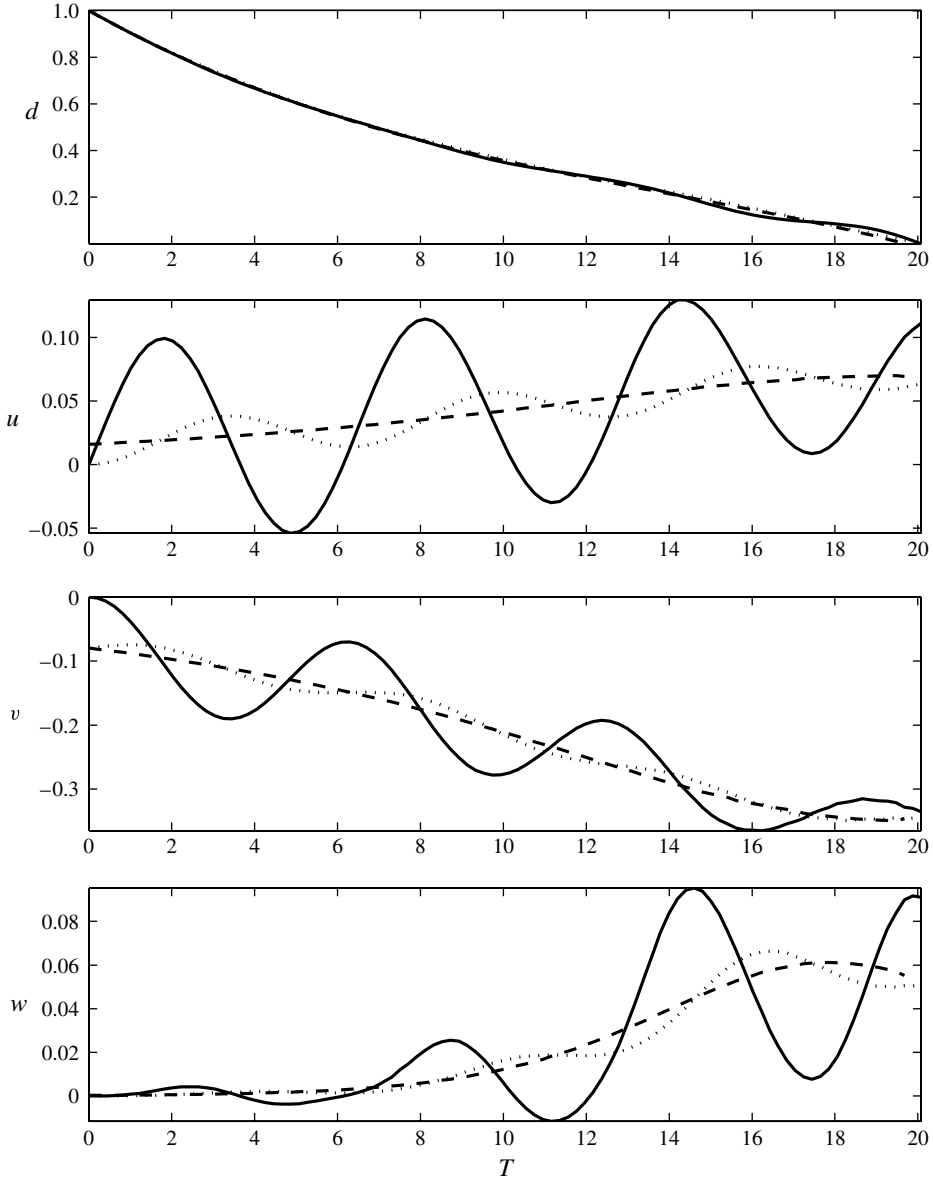


FIGURE 2. Time series of the frontal width d and the perturbation velocity magnitudes (u , v , w) at the x position of the buoyancy gradient maximum (the front) for parameter values of $\delta = 0.1$ and $Ro = 0.4$. The vertical position is $z = 0$ for the horizontal velocities u and v , and $z = 1/2$ for the vertical velocity w . The general solution (3.4) is shown for a full mass imbalance $\epsilon = 1$ (solid) and zero initial imbalance $\epsilon = 0$ (dotted). The HB72 solution given by (3.5c) is also shown (dashed).

variables for an arbitrary mass imbalance ϵ is a factor of ϵ/δ larger than for the initially balanced case.

The effect of the initial conditions on the in-plane flow (u , w) is greater than on the along-front flow for both balanced and unbalanced initial conditions. This may be understood by observing that while the oscillation amplitudes in u (3.4b) and w (3.4c)

are of a similar order to those in v , the in-plane flow from the HB72 solution is a factor of δ smaller than the along-front flow (this is true regardless of the size of the Rossby number). Furthermore, in figure 2 the oscillations in the vertical velocity grow up to about $T = 15$ as a result of the deformation field amplifying the vertical flow (including the oscillatory component: see the expression for the vertical velocity (3.4c)). This effect is far less noticeable (but still present) when the system starts in a geostrophically balanced state. Given these results we conclude that the HB72 model is a good predictor of the buoyancy field for even quite large Rossby numbers (as long as $Ro^2/2 \ll 1$) regardless of the initial conditions, but is substantially poorer at describing the velocity fields, particularly when the initial state is unbalanced. Specifically, the semigeostrophic assumption of a geostrophic along-front velocity (i.e. $v \simeq v_g$) is reasonable only for (i) small initial imbalances ($\epsilon \ll 1$), and (ii) sufficiently small Rossby numbers ($Ro \ll Ro_c/\sqrt{2}$) such that the inertial oscillations do not themselves cause frontogenesis.

4. Geostrophic adjustment and frontogenesis in uniform PV flow

We now use the framework developed in § 2 to analyse the fully time-dependent adjustment and frontogenesis problem in uniform PV flow with initial conditions of zero motion. In § 4.1 we examine the unforced system, $\delta = 0$, before moving on to the more general case of $\delta \neq 0$ in § 4.2. To simplify the analysis it is useful to take the (complex) Fourier transform in X and cosine transform in Z (to satisfy the rigid lid boundary conditions) of the linearized governing differential equation (2.38). Equation (2.38) then becomes

$$\frac{\partial^2 \widehat{v}}{\partial T^2} + \widehat{v} \left(1 - \delta^2 + \left(\frac{kBu}{n\pi} e^{\delta T} \right)^2 \right) = -ik A_n Ro \widehat{b}_0 e^{\delta T}, \tag{4.1}$$

where k is the horizontal wavenumber, n the vertical wavenumber, hats denote Fourier mode amplitudes defined by

$$\widehat{v} = \int_{-\infty}^{\infty} v e^{ikX} dX, \tag{4.2}$$

and A_n is defined by the Fourier series,

$$\sum_{n=1}^{\infty} A_n \cos n\pi Z = \left(Z - \frac{1}{2} \right) \Rightarrow A_n = \frac{2(-1 + (-1)^n)}{n^2 \pi^2}. \tag{4.3}$$

Similar transformation of the equations for the other field variables (2.29), (2.30), (2.33) and (2.26) yields

$$\widehat{w}_* = \frac{-ik}{n\pi} \left(\delta \widehat{v} + \frac{\partial \widehat{v}}{\partial T} \right), \tag{4.4a}$$

$$\widehat{\psi} = \frac{-1}{n\pi} \left(\delta \widehat{v} + \frac{\partial \widehat{v}}{\partial T} \right), \tag{4.4b}$$

$$\widehat{u}_* = - \left(\delta \widehat{v} + \frac{\partial \widehat{v}}{\partial T} \right), \tag{4.4c}$$

$$\widehat{\Delta b} = \frac{ik Ro}{n\pi F^2} e^{\delta T} \widehat{v}. \tag{4.4d}$$

Note that the (effective) horizontal velocities (u_* and v) involve cosine modes in the vertical, while the effective vertical velocity (w_*), cross-front streamfunction (ψ), and buoyancy anomaly (Δb) involve sine modes.

Equation (4.1) is a simple constant coefficient ordinary differential equation (ODE) when $\delta = 0$ and is solved analytically below (§ 4.1). However when $\delta \neq 0$, (4.1) is a variable coefficient second-order ODE in time, and is therefore solved numerically (in MATLAB) for the cases studied below (§ 4.2).

4.1. Uniform PV flow with no deformation field

For uniform PV flow in the absence of a deformation field the solution to the mass imbalance problem is given by (4.1) with δ set to zero,

$$\frac{\partial^2 \widehat{v}}{\partial T^2} + \omega^2 \widehat{v} = -ik A_n Ro \widehat{b}_0, \quad (4.5)$$

with frequency ω defined by

$$\omega(k, n) = \sqrt{1 + \left(\frac{kBu}{n\pi}\right)^2}. \quad (4.6)$$

Following B00, we apply initial conditions of zero motion, $u = v = w = 0$, or equivalently

$$v = \frac{\partial v}{\partial T} = 0, \quad (4.7)$$

via substitution into the expression for u (2.31). Solving (4.5) with these initial conditions results in

$$\widehat{v} = -\frac{ik \widehat{b}_0 A_n Ro}{\omega^2} (1 - \cos \omega T). \quad (4.8a)$$

The other fields are generated by substitution of (4.8a) into (4.4c,a,d):

$$\widehat{u}_* = ik \widehat{b}_0 Ro \frac{A_n}{\omega} \sin \omega T, \quad (4.8b)$$

$$\widehat{w}_* = -\frac{k^2 \widehat{b}_0 A_n Ro}{n\pi\omega} \sin \omega T, \quad (4.8c)$$

$$\widehat{\Delta b} = \frac{k^2 \widehat{b}_0 A_n Bu^2}{n\pi\omega^2} (1 - \cos \omega T). \quad (4.8d)$$

As expected, the solution given by (4.8) reveals the existence of propagating inertia-gravity waves (IGWs). Equation (4.6) is equivalent to the usual hydrostatic IGW dispersion relation (e.g. equation (3) of Bouchut, Sommer & Zeitlin 2004) with dimensional gravity wave speed $c = NH/(n\pi)$. The IGW group velocity,

$$c_g = \frac{d\omega}{dk} = \frac{Bu^2 k}{n^2 \pi^2 \omega}, \quad (4.9)$$

is finite for all wavenumbers $k \neq 0$ as long as Bu is non-vanishing. Given this group velocity in momentum coordinates, the position of a wave at time T (sourced from the origin at time zero) will be $X = c_g T$ in momentum coordinates and $x = c_g T - Ro v(c_g T, Z, T)$ in Eulerian coordinates. Since v is a sum of odd vertical

cosine modes, it is always identically zero at mid-depth ($z = 0.5$) and consequently the propagation distance is the same (i.e. $x \equiv X$) in both coordinate systems at this vertical height. The only difference between the dynamics of wave propagation in the two coordinate systems is that in Eulerian coordinates a given wave packet is tilted about $z = 0.5$ according to the vertical shear in the local along-front velocity $v(c_g T, Z, T)$. Thus the finite group velocity for $Bu \neq 0$ as per (4.9) implies that all wavenumbers $k \neq 0$ will propagate away from the imbalance region in finite time. Higher wavenumbers will propagate most rapidly, while smaller wavenumbers will propagate only very slowly. Since $\omega \rightarrow 1$ and $c_g \rightarrow 0$ for small k , the solution will exhibit slowly decaying near-inertial oscillations in the imbalance region due to the low wavenumber modes. The IGW signal in the above solution (4.8) is given by the transient (T -dependent) part. The steady or *geostrophically adjusted* final state, defined as the T -independent part of the solution, is given by

$$\widehat{u}_{ss} = 0, \tag{4.10a}$$

$$\widehat{v}_{ss} = -\frac{ik \widehat{b}_0 A_n Ro}{\omega^2}, \tag{4.10b}$$

$$\widehat{w}_{ss} = 0, \tag{4.10c}$$

$$\widehat{\Delta b}_{ss} = \frac{k^2 \widehat{b}_0 A_n Bu^2}{n\pi\omega^2}. \tag{4.10d}$$

The steady state defined by (4.10) is identical to the steady state solution derived by Blumen & Wu (1995, their equations (32) and (33)). As expected, the in-plane flow vanishes, leaving an out-of-plane geostrophic jet given by (4.10b) in balance with the steady state buoyancy field,

$$b_{ss}(X, Z) = b_0(X) + F^{-2}Z + \Delta b_{ss}(X, Z), \tag{4.11}$$

as may be confirmed by substitution of (4.10b) and (4.11) into the steady state thermal wind equation (from (2.19) with $v = v_g$):

$$\frac{\partial v_{ss}}{\partial Z} = Ro \frac{\partial b_{ss}}{\partial X}. \tag{4.12}$$

Given the above arguments with respect to wave propagation, the time scale for the geostrophic adjustment process may be estimated from the group velocity as the time taken for a typical mode (e.g. $k = n = 1$) to leave the imbalance region (roughly $|X| < 1$). Applying (4.9), the non-dimensional adjustment time scale is

$$\tau = \frac{1}{c_g} = \sqrt{1 + \left(\frac{\pi}{Bu}\right)^2}, \tag{4.13}$$

which is finite unless Bu is vanishingly small. The degree of geostrophic adjustment of the buoyancy field is also governed by the Burger number, with the steady state buoyancy anomaly (4.10d) becoming negligibly small for

$$Bu = \frac{NH}{Lf} \ll 1, \tag{4.14}$$

and thus the buoyancy field behaving similarly to the zero PV limit. In this limit the group velocity (4.9) approaches zero and the frequency (4.6) approaches one for all wavenumbers – that is, the solution becomes only weakly dispersive and near-inertial. In physical terms, the near absence of background stratification limits inertia–gravity

wave propagation and consequently much of the energy associated with the mass imbalance remains localized in the frontal region as an oscillating near-inertial wave for a significant period of time. The condition (4.14) is equivalent to the requirement that the length scale L is very much greater than the Rossby radius $L_R = NH/f$, and thus (4.14) is often termed the *large-scale limit*. In the extreme case of vanishing Burger number the solution collapses to the zero PV limit already considered in § 3, with the buoyancy anomaly vanishing entirely. In contrast, in the opposite extreme small-scale limit, the steady state velocity field vanishes ($v_{ss} = 0$) and the buoyancy anomaly exactly cancels the initial buoyancy field ($\Delta b_{ss} = -b_0$). One physical example of this limit is non-rotating flow ($f \rightarrow 0$) where the initial imbalance generates outward propagating gravity currents, leaving behind a stably stratified, motionless region. There is a continuum of behaviours between the zero PV extreme large-scale limit and this strongly dispersive extreme small-scale limit.

Let us now consider the occurrence of frontal discontinuities in uniform PV flow using solution (4.8). The general condition for singularity formation is that the inverse Jacobian (see table 1) vanish, or

$$J^{-1} = 1 - Ro \frac{\partial v}{\partial X} \leq 0. \quad (4.15)$$

Hence for a singularity to occur at a given Rossby number, the X derivative in the along-front flow v (which is zero at time zero) must become sufficiently large, $\partial_X v > 1/Ro$. This gradient will obtain its maximum value in the frontal zone as the unbalanced initial conditions drive wave generation and oscillations about the steady state. In the zero PV case ($Bu = 0$) where there is no energy loss from the frontal zone, the maximum value of the $\partial_X v$ is obtained at half an inertial period ($T = \pi$) as seen in § 3. For larger Bu the system becomes more dispersive and energy is lost from the frontal zone more rapidly, reducing the maximum gradient obtainable in the frontal zone and the time at which it occurs. Heuristically, we therefore expect that for larger Bu it becomes increasingly unlikely for $\partial_X v$ to exceed $1/Ro$ and thus for a singularity to form. More rigorously, (4.15) may be rewritten as

$$\mathcal{F}^{-1} \left[\sum_{n=1}^{\infty} (-ik Ro \hat{v}) \right] \geq 1, \quad (4.16)$$

with \mathcal{F}^{-1} denoting the inverse Fourier transform (and noting that $\cos n\pi Z = 1$ on the lower boundary). Equation (4.16) must be evaluated numerically for a given profile $b_0(X)$. We have evaluated (4.16) for the error function buoyancy profile defined by (3.12) and plotted the result in figure 3. We note that employing a different buoyancy profile does not significantly alter the result. With reference to figure 3, we now have a general description of how the formation of strong fronts (singularities) is controlled by stratification (Froude number) and rotation (Rossby number). The main features of figure 3 are as follows.

- (i) For a given Froude number there exists a critical Rossby number which must be exceeded for a singularity to occur, and this critical value is minimum in the absence of stratification.
- (ii) As F is decreased and the system becomes increasingly stratified, the Rossby number required for singularity formation increases since energy is removed more rapidly from the imbalance region via inertia–gravity wave propagation.

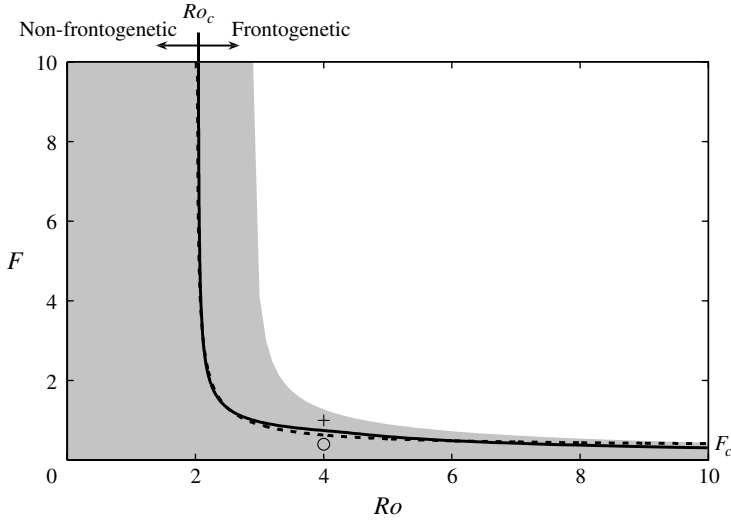


FIGURE 3. The limiting curve (solid) evaluated from (4.16) for the error function profile (3.12) dividing frontogenetic (above) and non-frontogenetic (below) regions. The limiting curve (dashed) found empirically by Neves (1996, equation (41)) from numerical simulations is also shown (rescaled appropriately to match the buoyancy profile given by (3.12)). The two specific cases of ($Ro = 4, F = 0.4$, non-frontogenetic) and ($Ro = 4, F = 1$, frontogenetic) considered in the text are represented by a circle and '+', respectively. The critical Rossby and Froude numbers, $Ro_c = 2.03$ and $F_c = 0.31$ respectively, are labelled. The shading indicates the parameter values for which an adjusted state (with non-vanishing inverse Jacobian) exists.

- (iii) There exists a critical Froude number F_c below which singularity formation is impossible regardless of the Rossby number (within the scope of the approximations made in our model): IGWs remove energy from the imbalance region too rapidly for a frontal singularity to form.

Also plotted in figure 3 is an empirical curve determined by Neves (1996), based on a suite of numerical simulations. The agreement between Neves' result and our analytical prediction is remarkable.

The set of Rossby and Froude numbers for which a continuous adjusted state exists has also been indicated in figure 3 (shaded grey). The curve bounding this existence region may be computed by replacing the velocity in the frontogenesis condition (4.16) with the steady state velocity from (4.10b). It is immediately apparent from figure 3 that the existence of a steady state with non-vanishing inverse Jacobian does not imply attainability of that state. Indeed, all sets of Rossby and Froude numbers in the shaded region above the critical curve (solid line) have corresponding steady states, but these states are never reached. Instead a singularity forms during the geostrophic adjustment process. The (Ro, F) parameter space is therefore divided into three regions based on the existence and attainability of an adjusted state: (i) for sufficiently small Rossby numbers a steady state does exist and is attainable; (ii) for sufficiently large Rossby numbers a steady state does not exist; and (iii) for intermediate Rossby numbers a steady state exists but is not attainable. In the case of zero PV flow ($F \rightarrow \infty$ in figure 3), it may be shown that the (critical) Rossby number required for singularity formation is a factor of $\sqrt{2}$ smaller than the Rossby

number required for the non-existence of the adjusted state (this result was previously derived by Blumen & Williams 2001). The three regions in the large-Froude-number limit are therefore as follows: for Rossby numbers in the range $Ro_c < Ro < \sqrt{2}Ro_c$ a steady state exists but is not attainable; for $Ro > \sqrt{2}Ro_c$ a steady state does not exist; for $Ro < Ro_c$ a steady state does exist and is attainable (at least in the limit of infinite time).

To illustrate the behaviour of the uniform PV solution (4.8) we examine the time evolution of the flow for the specific profile specified by (3.12) for two sets of parameters. Firstly, a *non-frontogenetic* case (i.e. no singularity forms) is considered ($Ro = 4$, $F = 0.4$, circle in figure 3) to demonstrate the dynamics of *small-scale* (since $Bu = 10$, or $L/L_R = 0.1$) geostrophic adjustment to a steady state. We plot the time evolution of the buoyancy field and along-front velocity field (figure 4), and the streamfunction (figure 5). The isopycnals in figure 4 flatten as an IGW is generated ($T = 0.5\pi$) before steepening again as the IGW propagates out of the imbalance region ($T = 0.75\pi$, π), but remaining flatter than in the initial state. An along-front jet rapidly develops with its maximum coincident with the horizontal buoyancy gradient maximum on the boundary. The jet magnitude oscillates near-inertially with time (e.g. see $T = 0, \pi, 2\pi, 3\pi$) as IGWs are generated. After only one inertial period ($T = 2\pi$) the buoyancy field attains a near-steady state in the frontal zone. IGWs continue to be generated and propagate away from the imbalance region but are of significantly smaller amplitude than the initial wave and thus not noticeable in the large-scale buoyancy field. The streamfunction in figure 5 initially ($T = 0.5\pi$) develops a single overturning cell in the imbalance region very similar to the zero PV case (for example, compare with figure 3 of B00). However, as IGWs are generated ($T \geq 0.75\pi$ in the figure) the strongest overturning is concentrated at the location of the outward propagating wavefronts, with a relatively weak (oscillating) overturning cell left behind in the imbalance region. The initial buoyancy field is plotted alongside the steady state buoyancy field, buoyancy anomaly, and geostrophic velocity in figure 7. The steady state fields are not substantially different from those at time $T = 9$ in figure 4.

A useful means to visualize the wave generation and propagation described above is through a Hovmöller plot of the streamfunction along $z = 0.5$, as shown in figure 6. As noted previously, this plot will look identical in momentum or Eulerian coordinates since $v \equiv 0$ and $x \equiv X$ along $z = 0.5$. Referring to figure 6, we observe that waves propagate away from the origin for all $T > 0$ with the smallest scales propagating most rapidly. The group velocity for waves with a vertical mode $n = 1$ and horizontal wavenumbers of $k = 0.1, 0.3$ and $k \rightarrow \infty$ are indicated using dashed lines. A given wave packet, seen as a coloured band in the figure, is composed of a range of wavenumbers and decays as it propagates outwards due to dispersion. This effect is also visible in the plots of the full streamfunction in figure 5. The propagation of the energy associated with the highest horizontal wavenumbers out of the frontal zone (approximately $|x| < 1$) rapidly leads (within an inertial period) to a decaying near-inertial oscillation in the frontal zone associated with the lowest horizontal wavenumbers.

For comparison with the above geostrophically adjusting case, the flow evolution for a frontogenetic case ($Ro = 4$, $F = 1$) is considered by way of the buoyancy field (figure 8) and along-front velocity field (figure 9). The key feature of these two figures (as compared with the non-frontogenetic case) is the rapid development of an infinite horizontal gradient (i.e. a frontal discontinuity) in the two fields. The increase in the Froude number as compared to the previous case (which had $F = 0.4$) decreases

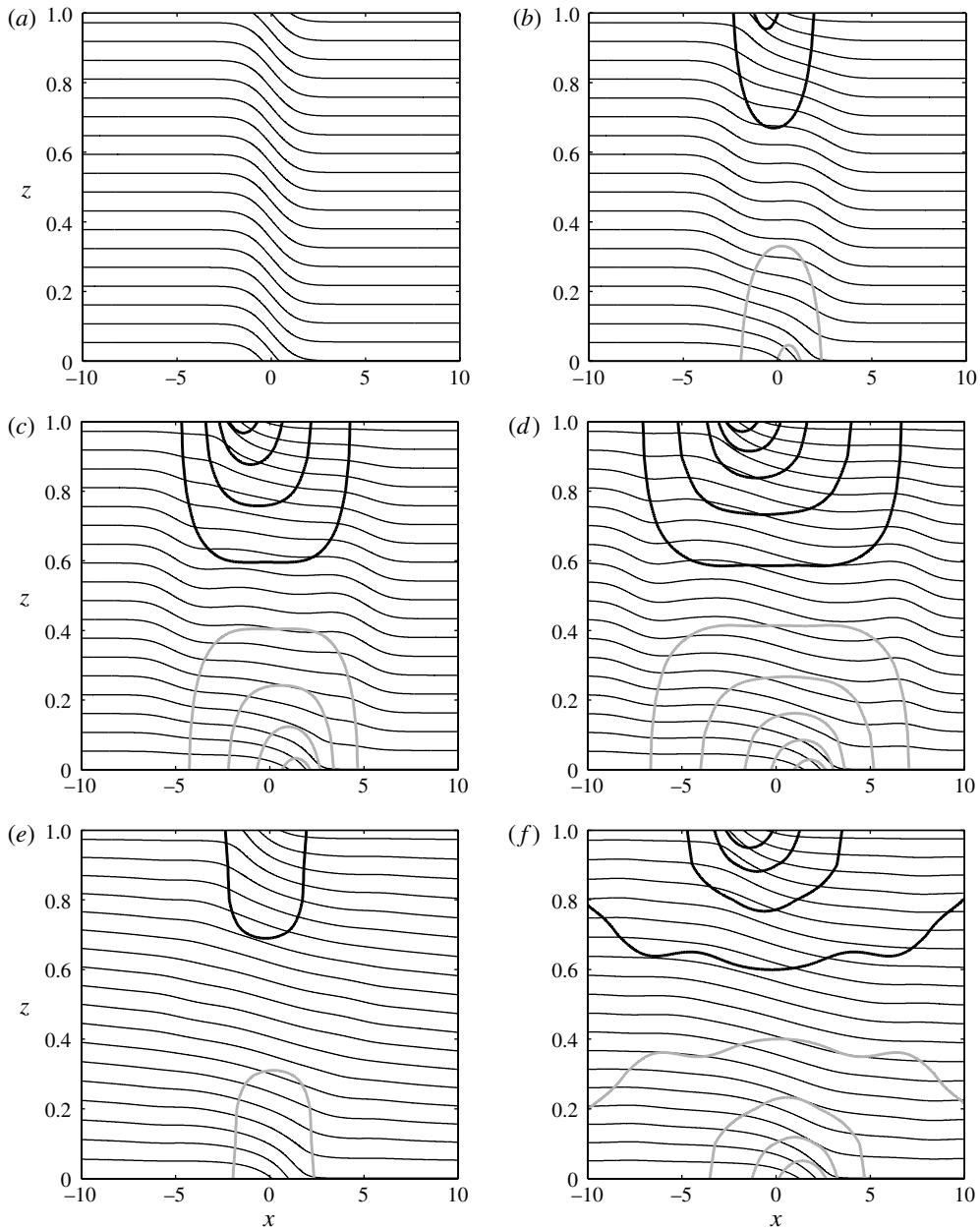


FIGURE 4. Geostrophic adjustment of the buoyancy (thin contours) and along-front velocity (thick contours) fields towards a steady state for (non-frontogenetic) initial parameter values of $Ro = 4$ and $F = 0.4$ ($\delta = 0$), as predicted by the general solution for uniform PV flow (4.8). Inertia-gravity waves propagate outward from the imbalance region leaving behind flatter isopycnals. Negative contours, denoting a velocity directed out of the page, are shown in grey. Contour intervals are 0.338 for the buoyancy and 0.1 for the velocity: (a) $T = 0$; (b) $T = 0.5\pi$; (c) $T = 0.75\pi$; (d) $T = 1\pi$; (e) $T = 2\pi$; (f) $T = 3\pi$.

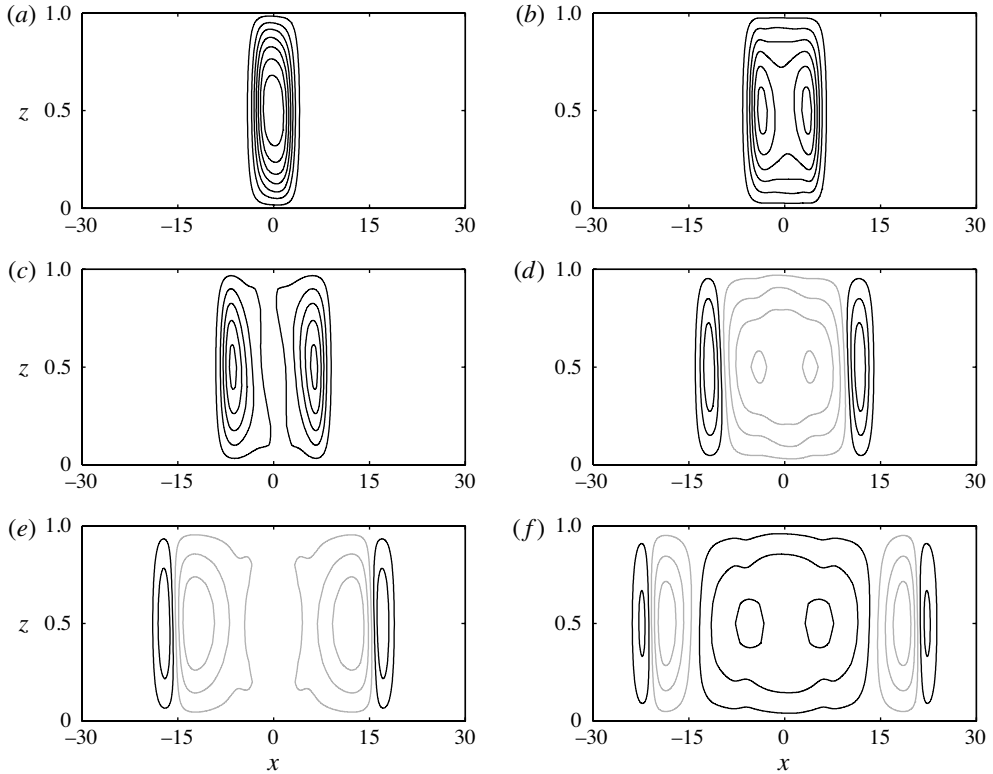


FIGURE 5. Time evolution of the streamfunction for initial parameter values of $Ro = 4$ and $F = 0.4$ ($\delta = 0$), as predicted by general solution for uniform PV flow (4.8). Inertia–gravity waves propagate outwards leaving a progressively weaker overturning cell in the initial imbalance region. Positive values (black) correspond to anticlockwise flow, and negative values (grey) to clockwise flow. Contour intervals are 0.01: (a) $T = 0.5\pi$; (b) $T = 0.75\pi$; (c) $T = 1\pi$; (d) $T = 1.5\pi$; (e) $T = 2\pi$; (f) $T = 2.5\pi$.

the propagation speed of IGWs, as previously discussed. Consequently energy cannot be dispersed away from the frontal zone sufficiently fast to prevent discontinuity formation. Note that the ‘+’ symbol denoting this frontogenetic case in figure 3 appears in the shaded region of the plot, implying that an adjusted state exists for the specified parameter values ($Ro = 4$, $F = 1$). However, the formation of a singularity during the geostrophic adjustment process, as seen in figures 8 and 9, prevents the system from attaining this steady state.

Figure 10 displays a time series of the frontal width d (as defined by (3.14)) and the Eulerian position x where the buoyancy gradient maximum occurs (i.e. the frontal position at time T) for both the frontogenetic and non-frontogenetic cases. Frontogenesis occurs when the frontal width vanishes, as happens within the first oscillation for the frontogenetic case. In the non-frontogenetic case the frontal width adjusts towards the steady state value of d represented by a dotted line in the figure. However, we observe that the minimum value of the frontal width, occurring during the first oscillation at about $T = 2$, is smaller than this steady state value. Generalizing this result, the sharpest front – and thus any discontinuity – will always occur during the first oscillation of the adjustment process, and can therefore prevent a system

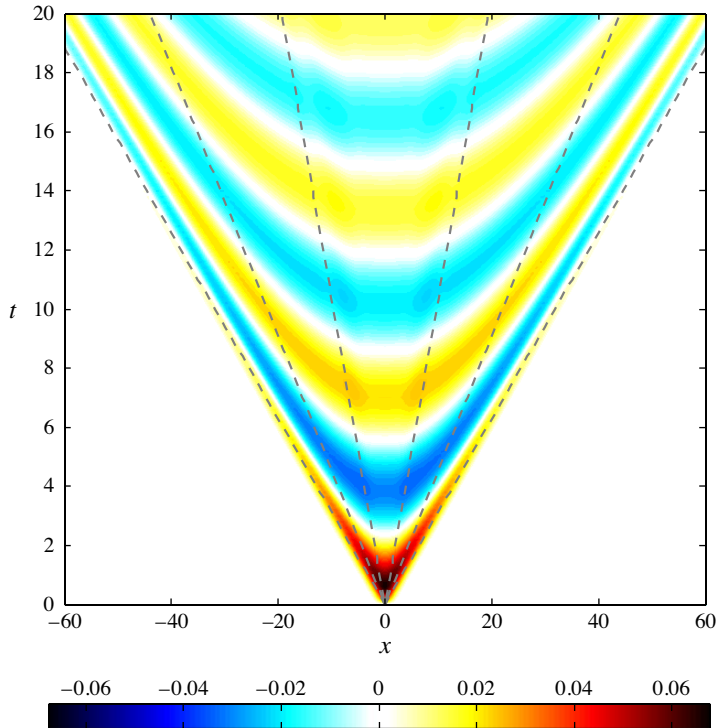


FIGURE 6. Hovmöller plot of the streamfunction at mid-depth $z = 0.5$ during the course of geostrophic adjustment for initial parameter values of $Ro = 4$ and $F = 0.4$ ($\delta = 0$), as predicted by general solution for uniform PV flow (4.8). The unbalanced initial conditions generate inertia–gravity waves which propagate outwards at a constant speed given by their group velocity, with the highest horizontal mode numbers propagating most rapidly. Group velocities for modes $n = 1$ and $k = 0.1, 0.3$ and $k \rightarrow \infty$ are indicated by dashed lines.

reaching the steady state (as previously discussed). Consistent with the Hovmöller plot in figure 6, the oscillations in the frontal width and position are (except for the first oscillation) close to inertial and decay slowly in time. Lastly, in figure 11 we plot time series for the three velocity components at the position of the front (that is, the position x plotted in figure 10), at three vertical levels. The oscillations in horizontal velocities are near-inertial, with the upper and lower boundaries 180° out of phase but with greater magnitudes at the lower boundary (where the front is located). As should be expected from the form of the solution (4.8), the velocities u and v are 90° out of phase on the boundaries. The vertical velocity w is maximum at the mid-level $z = 1/2$ and decays very rapidly in time in comparison to the horizontal velocities, although again oscillating with a near-inertial period.

4.2. Uniform PV flow with a deformation field

In this section we will consider the limit of frontogenesis *forced* by a background strain flow in the general case of uniform (non-zero) PV. The general linearized equation for uniform PV flow subject to a deformation field is given by (4.1). The generalized model permits arbitrary initial conditions for the buoyancy and along-front velocity, as long as they correspond to uniform PV. Here we will consider two

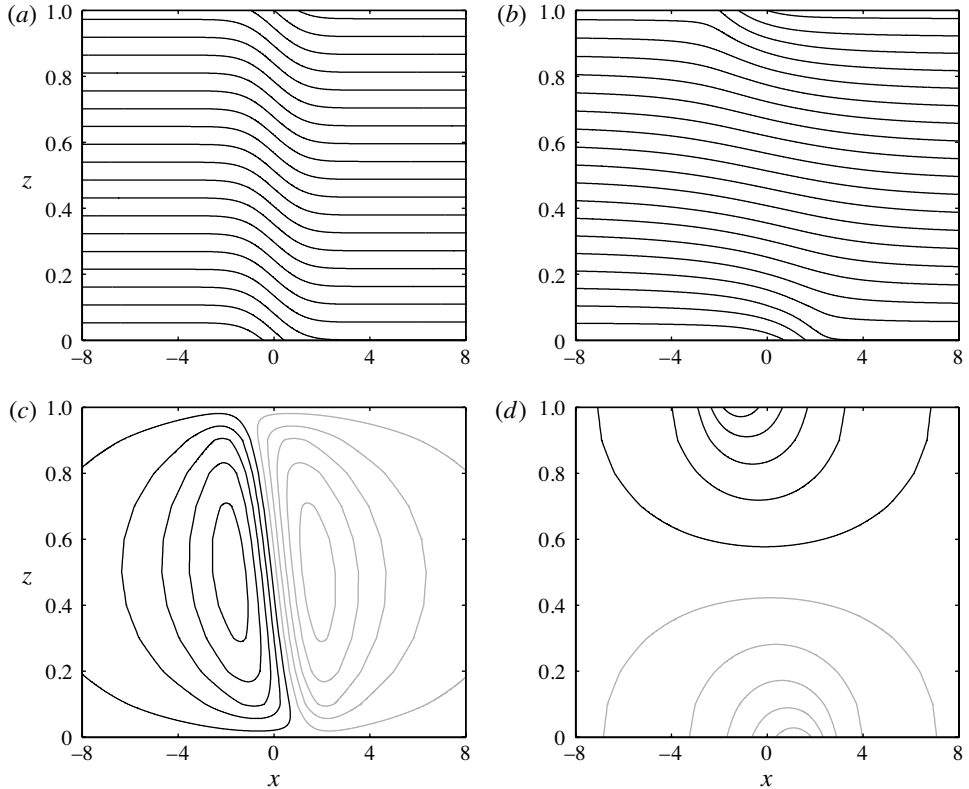


FIGURE 7. The initial buoyancy field (a) for parameter values of $Ro = 4$ and $F = 0.4$ ($\delta = 0$), and the corresponding geostrophically adjusted steady state as predicted by (4.10). The isopycnals are flattened in the steady state (b) relative to the initial configuration and in balance with a steady geostrophic out-of-plane jet (d). The buoyancy anomaly pertaining to the geostrophically adjusted state is also shown (c). Negative contours are shown in grey. Contour intervals are 0.338 for the buoyancy, 0.06 for the buoyancy anomaly and 0.061 for the velocity: (a) b_0 ; (b) b_{ss} ; (c) Δb_{ss} ; (d) v_{ss} .

particular initial conditions: (i) unbalanced initial conditions, defined as

$$\widehat{v}(0) = \frac{\partial \widehat{v}(0)}{\partial T} = 0; \quad (4.17)$$

and (ii) geostrophically balanced initial conditions, defined as

$$\widehat{v}(0) = \widehat{v}_{ss}, \quad \frac{\partial \widehat{v}(0)}{\partial T} = -\delta \widehat{v}_{ss}, \quad (4.18)$$

where the velocity \widehat{v}_{ss} is given by (4.10b). Initial condition (i) implies no anomalous flow at time zero, $u = v = w = 0$, such that only the large-scale strain flow is present. Initial condition (ii) implies a geostrophically balanced along-front velocity, $v = v_g$, but zero in-plane anomalous flow (e.g. from (4.4b)), $u = w = 0$. However, before considering the effect of initial conditions let us examine the long-time limit of (4.1) for small strain. At large times $T \gg 1$ we assume that the only time dependence in the along-front flow arises via the strain field (since all oscillations are presumed to have decayed away) and hence that $\partial_{TT} v = O(\delta^2 v)$. Further assuming that $\delta \ll 1$, we obtain

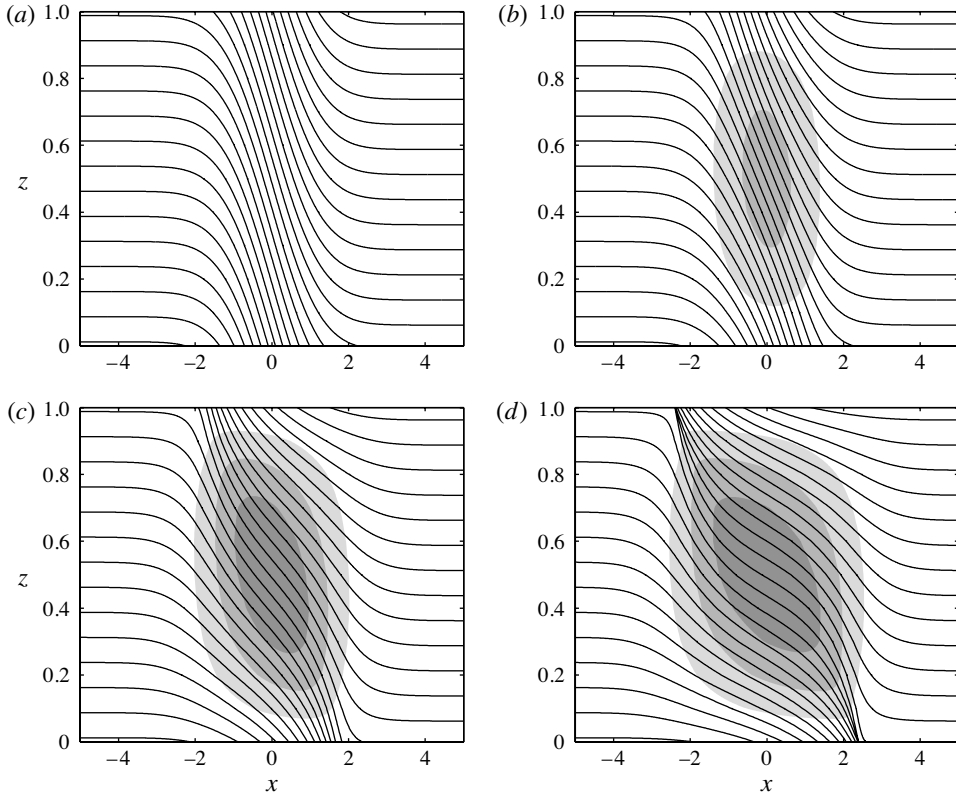


FIGURE 8. Time evolution of the buoyancy field for initial parameter values of $Ro = 4$ and $F = 1$ ($\delta = 0$), as predicted by general solution for uniform PV flow (4.8). An infinite horizontal buoyancy gradient develops on the upper and lower boundaries. The streamfunction (anticlockwise) at each time is represented by grey shading. Contour intervals are 0.075 for the buoyancy and 0.006 for the streamfunction: (a) $T = 0$; (b) $T = 0.42$; (c) $T = 0.87$; (d) $T = 1.32$.

a simplified version of (4.1),

$$\hat{v} \left(1 + \left(\frac{kBu}{n\pi} e^{\delta T} \right)^2 \right) = -ik A_n Ro \hat{b}_0 e^{\delta T}, \quad (4.19)$$

where A_n is defined by (4.3). Equation (4.19) is a Fourier representation equivalent to HB72's equation (2.42). The along-front flow is therefore

$$\hat{v} = -ik A_n Ro \hat{b}_0 e^{\delta T} \left(1 + \left(\frac{kBu}{n\pi} \right)^2 e^{2\delta T} \right)^{-1}. \quad (4.20a)$$

The cross-front streamfunction and buoyancy anomaly may be expressed using (4.4) as

$$\hat{\psi} = ik Ro \frac{2A_n \delta \hat{b}_0}{n\pi} e^{\delta T} \left(1 + \left(\frac{kBu}{n\pi} \right)^2 e^{2\delta T} \right)^{-2}, \quad (4.20b)$$

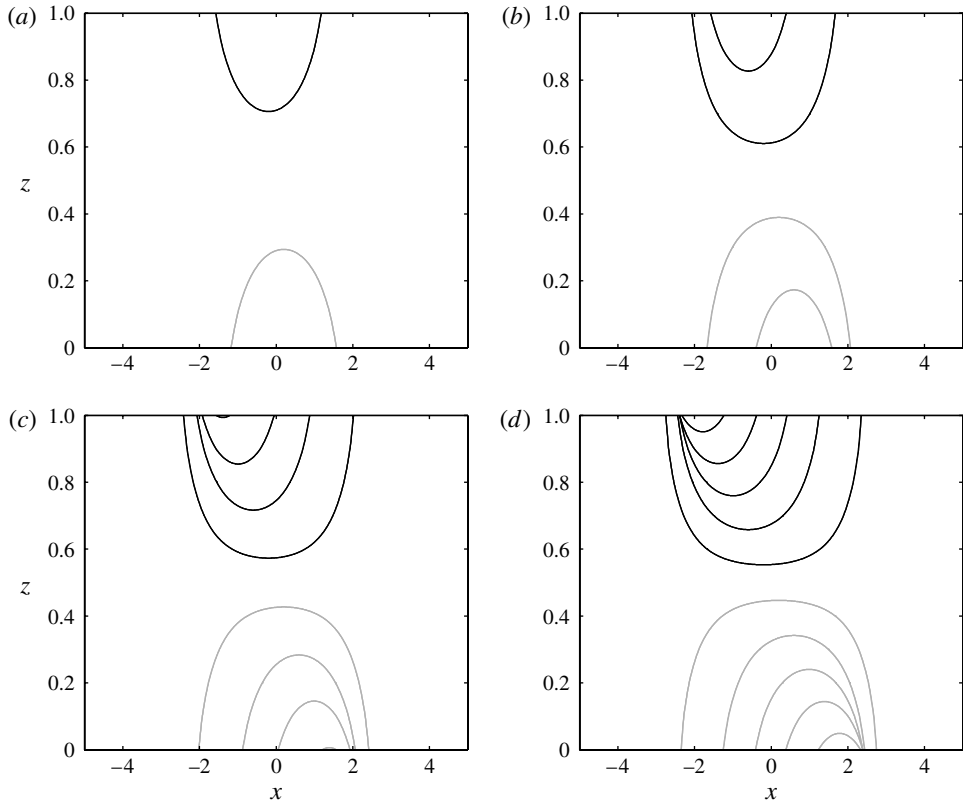


FIGURE 9. Time evolution of the along-front (out-of-plane) velocity field for initial parameter values of $Ro = 4$ and $F = 1$ ($\delta = 0$), as predicted by general solution for uniform PV flow (4.8). The baroclinic jet intensifies with time and develops an infinite horizontal gradient on the upper and lower boundaries as frontogenesis occurs. Negative contours are shown in grey. Contour intervals are 0.1: (a) $T = 0.57$; (b) $T = 0.81$; (c) $T = 1.05$; (d) $T = 1.32$.

$$\widehat{\Delta b} = \frac{k^2 Bu^2 A_n \widehat{b}_0}{n\pi} e^{2\delta T} \left(1 + \left(\frac{kBu}{n\pi} \right)^2 e^{2\delta T} \right)^{-1}. \quad (4.20c)$$

This solution (4.20) is equivalent to the uniform PV solution of HB72 (their equations (3.51), (3.52) and (3.54)), although their solution is expressed differently. As discussed in the zero PV case, the assumption of a long-time solution and associated neglect of the oscillatory part of the flow in (4.19) constrains the range of parameter values for which the equation (and consequently the model of HB72) is valid. A bounding constraint is that the initial state implied by the HB72 solution must be continuous with a non-vanishing inverse Jacobian. Since the initial condition implied by the HB72 model (e.g. by evaluating (4.20a) at $T = 0$) is that of geostrophic balance, the model can only be valid for parameter values (Ro, F) where this geostrophically balanced state exists as a uniform PV model solution. This region of existence was found in the previous section (§ 4.1) and shown as the shaded region in figure 3. Thus the uniform PV HB72 solution, like the zero PV HB72 solution (see § 3), is only valid for sufficiently small (but still order-one) Rossby numbers. With reference to figure 3, the

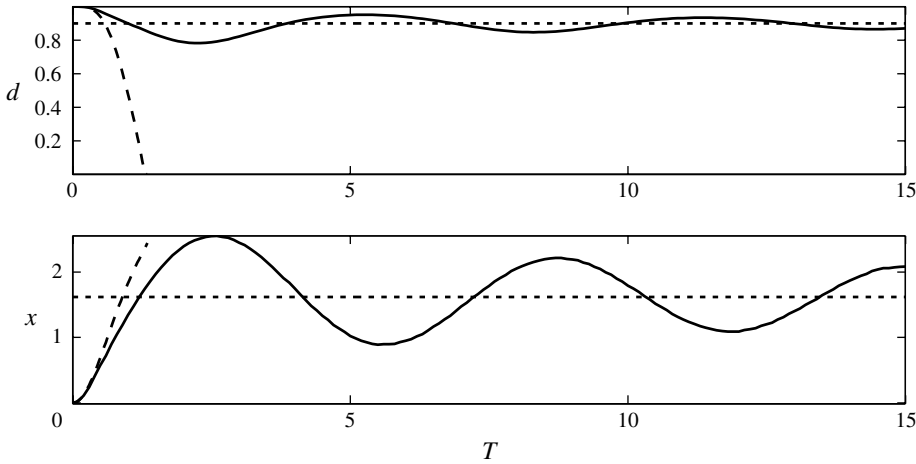


FIGURE 10. Time series of the frontal width d and frontal position x (the position of the buoyancy gradient maximum on the lower boundary), for the non-frontogenetic ($Ro = 4, F = 0.4, \delta = 0$, solid) and frontogenetic ($Ro = 4, F = 1, \delta = 0$, dashed) cases, as predicted by the uniform PV solution (4.8). The steady state frontal width and position predicted by (4.10) are also shown as dotted lines for the non-frontogenetic case.

range of Rossby numbers for which the HB72 solution is valid increases for smaller Froude numbers (stronger stratification).

Let us now consider the full solution to the uniform PV deformation frontogenesis problem including wave motions. To do this it is convenient to rewrite the full linearized equation (4.1) for $\delta \neq 0$ and finite Bu with a change of variable, $T \rightarrow \eta$, with

$$\eta = \frac{kBu}{\delta n\pi} e^{\delta T}. \tag{4.21}$$

Equation (4.1) then becomes a forced Bessel equation,

$$\eta^2 \frac{\partial^2 \hat{v}}{\partial \eta^2} + \eta \frac{\partial \hat{v}}{\partial \eta} + \hat{v} (\eta^2 + \delta^{-2} - 1) = \frac{-i A_n Ro n \pi \hat{b}_0}{\delta Bu} \eta, \tag{4.22}$$

the solution to which may be written as the sum of a forced part \hat{v}_F and wave components,

$$\hat{v} = \hat{v}_F + c_1(k, n) J_\sigma(\eta) + c_2(k, n) Y_\sigma(\eta), \tag{4.23}$$

where $J_\sigma(\eta)$ and $Y_\sigma(\eta)$ are the Bessel functions of complex order $\sigma = \sqrt{1 - \delta^{-2}}$. The expression for the forced component \hat{v}_F involves integrals of Bessel functions and will not be detailed here. However, when $\delta \ll 1$ the leading-order term in the forced component is simply given by the HB72 solution from (4.20a) and the order of the Bessel functions becomes $\sigma = i/\delta$. The constants c_1 and c_2 may be determined for each mode (k, n) for unbalanced or geostrophically balanced initial conditions using (4.17) or (4.18), respectively. As before, the other flow fields can then be calculated from v using (4.4). For either set of initial conditions, the flow is composed of an IGW field associated with the Bessel functions in (4.23), which drives oscillations about a time-varying mean state given by the HB72 solution.

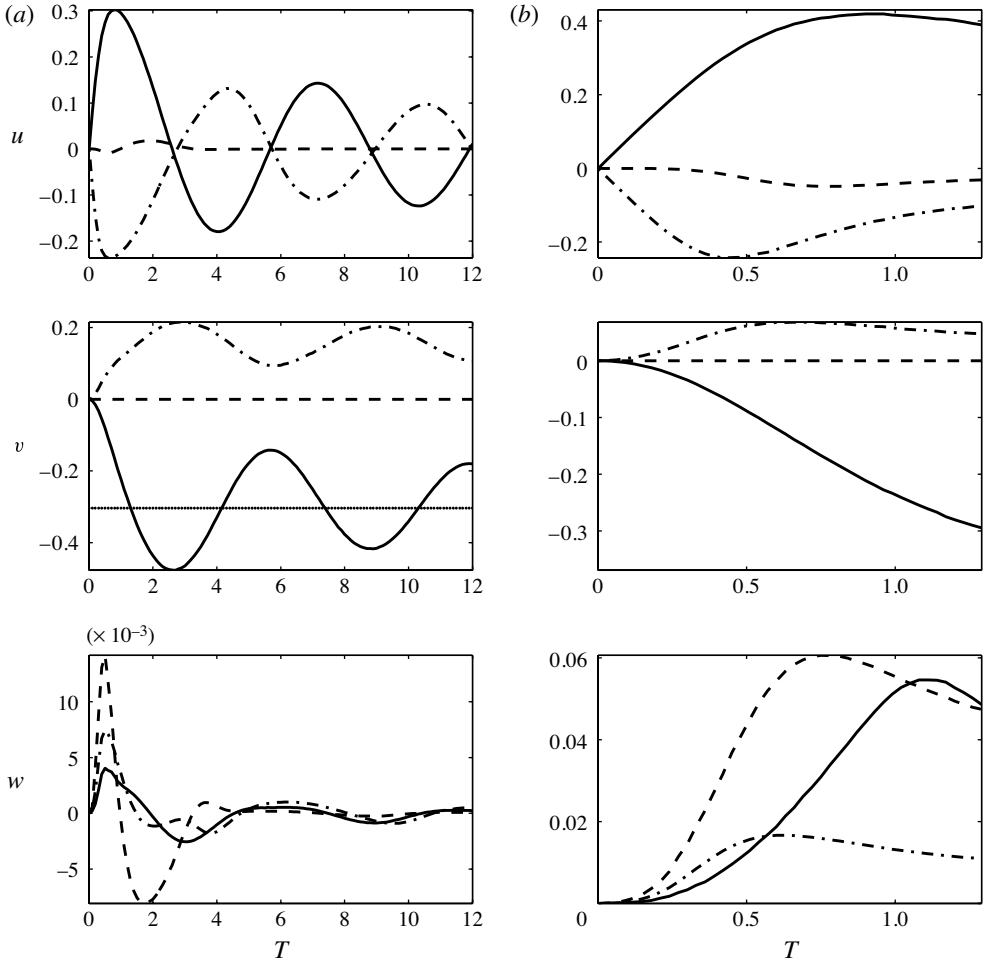


FIGURE 11. Time series of the velocity magnitudes (u, v, w) at the position of the buoyancy gradient maximum on the lower boundary for three vertical heights, for (a) the non-frontogenetic ($Ro = 4, F = 0.4, \delta = 0$) and (b) frontogenetic ($Ro = 4, F = 1, \delta = 0$) cases. For the horizontal velocities u and v the heights are $z = 0$ (solid), $z = 0.5$ (dashed) and $z = 1$ (dot-dashed). For the vertical velocity w the heights are $z = 0.1$ (solid), $z = 0.5$ (dashed) and $z = 0.9$ (dot-dashed). Also shown (dotted) is the steady state maximum value of v on the lower boundary, as predicted by (4.10).

Using the solution (4.23) we can describe the dynamics of the inertia-gravity waves. The mode number dependence of the Bessel functions may be fully described by a single parameter $a = kBu/(n\pi)$. We consider the two extreme limits of $\eta \rightarrow 0$ and $\eta \rightarrow \infty$ using the first term in a series expansion of $J_\sigma(\eta)$:

$$J_\sigma\left(\eta = \frac{a}{\delta}e^{\delta T}\right) \rightarrow \begin{cases} h(\delta, a)e^{iT} & \eta \rightarrow 0, \\ g(\delta, a)e^{-(\delta/2)T} \sin\left(\frac{a}{\delta}e^{\delta T} + \phi(a, \delta)\right) & \eta \rightarrow \infty, \end{cases} \quad (4.24)$$

where h, g and ϕ are unspecified functions. Note that a similar result applies for the other Bessel function, $Y_\sigma(\eta)$. In the limit of small η the Bessel mode reduces to

a non-propagating inertial wave ($\omega = 1, c_g = 0$) with constant amplitude. In contrast, for large η the Bessel function has an exponentially increasing frequency and group speed (in momentum coordinates) and its amplitude decays at a rate of $\delta/2$. The initial behaviour of a given wave packet will depend on the value of a associated with it, since the initial value of η is $\eta_0 = a/\delta$. Waves with $\eta_0 = kBu/(n\pi\delta) \gg 1$ will begin to both propagate and decay immediately. Waves with $\eta_0 \ll 1$ will be trapped in the frontal zone as oscillating inertial waves at early times. However, at some point in time (presuming a discontinuity does not occur first) η will grow sufficiently large that the waves will begin to propagate and decay (as per the large η limit). The time at which the waves are released may be estimated based on the time at which higher-order terms in the small η series given in (4.24) become comparable to the first term. Using this method, the time at which a wave begins to propagate and decay is

$$\delta T_R \simeq \ln \frac{\sqrt{\delta}}{a} = \ln \frac{n\pi\sqrt{\delta}}{kBu}. \tag{4.25}$$

We call T_R the *release time*. Larger horizontal wavenumbers and smaller vertical wavenumbers are released more rapidly, and if $kBu/(n\pi\sqrt{\delta}) \geq 1$ the release is immediate ($T_R = 0$). Since wavenumbers $k \sim 1$ will be the most energetic for an appropriately scaled buoyancy gradient profile $b'_0(X)$, a good estimate for the earliest time of release for energetic (observable) waves is given by setting $k = n = 1$ and thus $T_R \sim \ln(\pi\sqrt{\delta}/Bu)$.

Now consider what happens to propagating waves in the limit of large time. Using (4.24) with $\eta \rightarrow \infty$, and interpreting the time-dependent argument of the sine function as the time integral of the frequency, $a \exp(\delta T)/\delta = \int \omega dT$, the frequency of the waves at time T is $\omega \approx Bu/(n\pi)k \exp \delta T$ in generalized momentum coordinates. In physical/Eulerian coordinates the frequency will be different since the mode number k_E increases exponentially due to the action of the strain field; that is, at mid-depth ($v = 0$),

$$x = e^{-\delta T} X \Rightarrow k_E = e^{\delta T} k \Rightarrow \omega = \frac{Bu k_E}{n\pi}. \tag{4.26}$$

The group speed of the waves in Eulerian coordinates thus approaches a constant value for all horizontal scales, $c_g = Bu/(n\pi)$. Waves with this group speed will propagate outwards into the strain flow (which has a non-dimensional velocity $U = -\delta x$) until they reach a point where their outward group velocity equals the inward strain flow velocity and they become stationary. From this argument the location at which the waves stagnate, x_s , is

$$x_s = \frac{Bu}{\delta n\pi}. \tag{4.27}$$

The amplitude of the waves continues to decay, and their scale $1/k_E$ to shrink, during this process. The decay time scale of the waves as a function of the parameter a is shown in figure 12 in terms of the time taken for the waves to decay to half their initial magnitude. As predicted from the above series expansion, the decay time scale approaches $2/\delta$ for large a and infinity for small a . The damping of IGWs by the action of frontogenetic strain has been described in a similar context by Thomas (2012).

The time dependence of the amplitude and frequency of the IGWs has important consequences for the wave action. The wave action, defined by $\mathcal{A} = E/\omega$ where E is the wave energy density, is a conserved quantity in classical models involving slowly

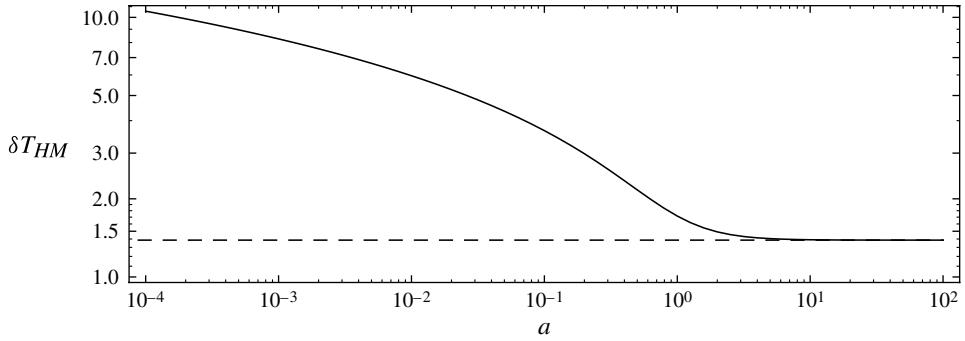


FIGURE 12. The scaled time taken δT_{HM} for the propagating wave components of the solution (4.23), $J_\sigma(\eta)$ and $Y_\sigma(\eta)$, to decay to half their initial magnitude in the small strain limit, $\sigma = 1/\delta$, in terms of the parameter $a = kBu/(n\pi)$. In the limit of large a the time taken δT_{HM} converges to $2 \ln 2$, corresponding to a decay rate of $\delta/2$.

varying, small-amplitude waves (see e.g. Bretherton & Garrett 1969). As already discussed above, here we see a decrease in amplitude and an increase in frequency of the waves in generalized momentum coordinates at large time; the wave amplitude A scales with $\exp(-\delta T/2)$ and the wave frequency with $\exp(\delta T)$ at large time (see (4.24)). The wave action therefore decays with time: $\mathcal{A} \sim A^2/\omega \sim \exp(-2\delta T)$. Thomas (2012) obtained a similar result of non-conservation of wave action under conditions of frontogenesis. This decay of wave action contrasts with the wave-capture paradigm of Buhler & McIntyre (2005), where the action is conserved and the wave amplitude grows exponentially, resulting in breaking and dissipation. Preliminary investigation indicates that both the decay and amplification paradigms are possible in a strained frontal flow depending on the source of the waves – a topic that will be studied in more detail in a future work.

We now consider an explicit example of strain-forced frontogenesis with parameter values of $Ro = 0.4$, $F = 0.8$ (hence $Bu = 0.5$, or $L/L_R = 2$) and $\delta = 0.1$. The results presented are derived from a direct numerical solution to (4.1) for each mode. In figure 13 we display the buoyancy field and streamfunction at the critical time for this set of parameter values for both balanced and unbalanced initial conditions. The major difference is a significantly stronger wave field in the latter case, associated with the large initial imbalance and subsequent geostrophic adjustment. Figure 14 shows a time series of the frontal width and position. The frontal width arising from the full solution (unbalanced, solid; balanced, grey) is almost indistinguishable from the HB72 solution (dashed). In contrast, the frontal position exhibits slowly decaying near-inertial oscillations about a ‘mean state’, as in the previous section. In this case the mean state is time-varying, and for the above parameter values is well described by the HB72 solution. The amplitude of the oscillations about the HB72 solution is far larger for the unbalanced solution and there is a 90° phase difference compared with the balanced solution. The balanced solution for the frontal position becomes visually indistinguishable from the HB72 solution at large time ($T \sim 20$).

The dynamics of the generated inertia–gravity waves seen in figure 13 are most transparent when the time-varying mean state (in this case the HB72 solution) is subtracted from the fields. Figure 15 displays a Hovmöller plot of the difference between the generalized model and the HB72 streamfunction, $\psi - \psi_{HB}$, at height $z = 0.5$ for unbalanced initial conditions. Using this figure we can trace the evolution

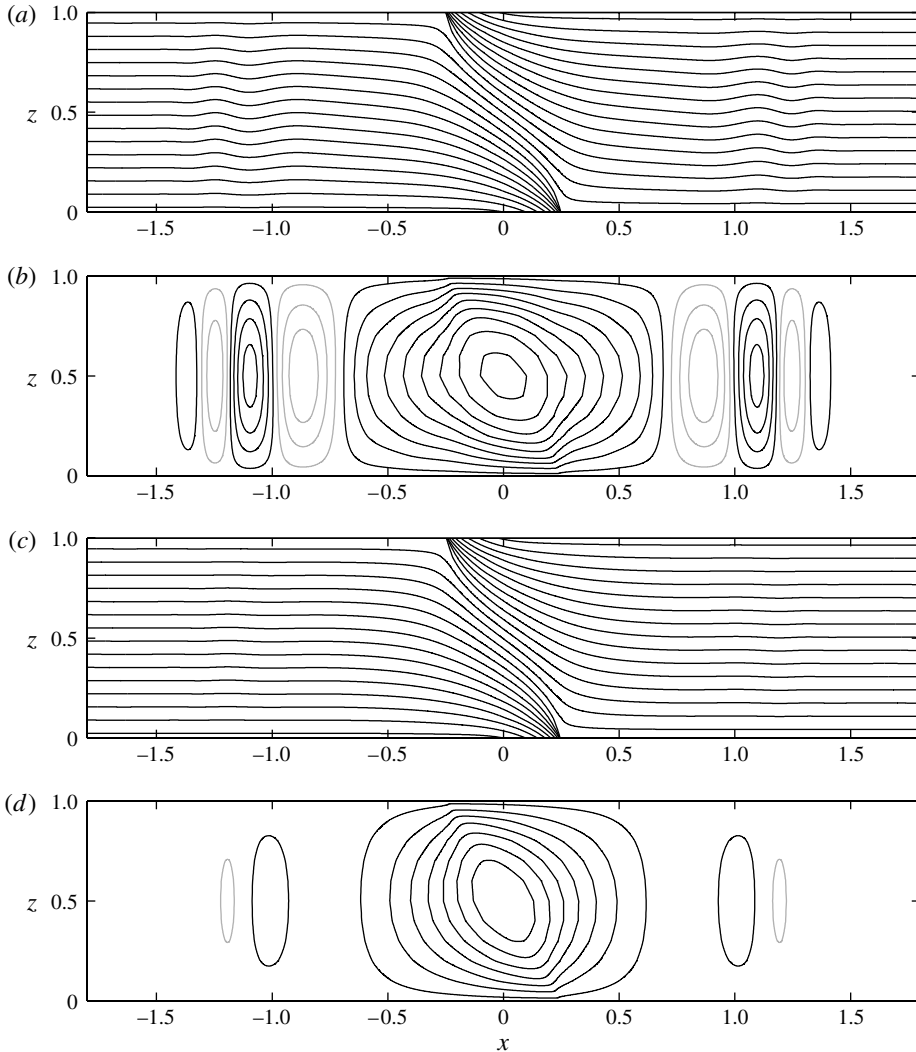


FIGURE 13. The buoyancy field and streamfunction at the critical time $t_c \approx 26$ for parameter values of $Ro = 0.4$, $F = 0.8$ and $\delta = 0.1$, as computed from the differential equation (4.1). Both unbalanced (*a,b*) and balanced (*c,d*) initial conditions are shown, with the same contour levels. The inertia-gravity wave field is substantially more intense for the unbalanced initial conditions. Positive values of the streamfunction (black) correspond to anticlockwise flow and negative values (grey) to clockwise flow. Contour intervals are 0.103 for the buoyancy and 0.002 for the streamfunction: (*a*) unbalanced, b ; (*b*) unbalanced, ψ ; (*c*) balanced, b ; (*d*) balanced, ψ .

of a given wave packet as seen in Eulerian coordinates (figure 15*a*) and generalized momentum coordinates (figure 15*b*). As predicted, the generated waves are trapped as inertial oscillations in the imbalance region until the release time ($T_R \simeq 7$ in this case, shown as a horizontal dashed line in the figure). The width of the oscillating region in Eulerian space begins to shrink due to the action of the strain field during this time, $T < T_R$. For $T > T_R$, waves begin to propagate outwards but with their

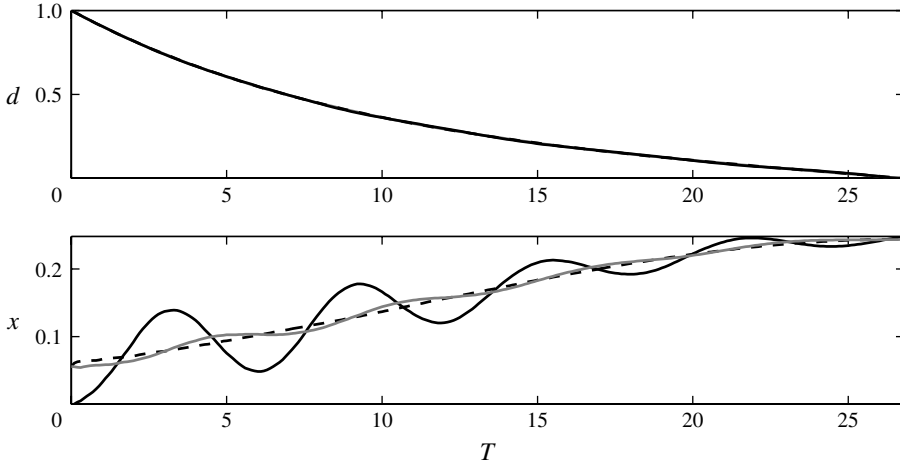


FIGURE 14. Time series of the frontal width d and frontal position x (the position of the buoyancy gradient maximum on the lower boundary), for parameter values of $Ro = 0.4$, $F = 0.8$ and $\delta = 0.1$, as computed from the HB72 solution ((4.20), dashed) and the differential equation (4.1) for both unbalanced (black solid) and balanced (grey solid) initial conditions.

propagation speed decreasing with time until they stagnate. The stagnation points x_s for the first vertical mode are shown by vertical dashed lines. The decay in wave amplitude with time predicted above is visible in both the Eulerian and momentum coordinate plots. Note that the horizontal scale of the waves in momentum coordinates (figure 15b) is approximately constant with time as they propagate, but shrinks in Eulerian coordinates (figure 15a) due to the squeezing effect of the strain field. Comparing the Hovmöller plot from §4.1 (figure 6) with the current figure, note that there is no trapping effect in the unstrained case ($T_R \rightarrow 0$) and waves begin to propagate immediately at time zero. Also, in the absence of strain, the waves propagate freely towards $\pm\infty$ rather than stagnating at $\pm x_s$.

5. Discussion and conclusions

We have developed a generalized model for frontogenesis which includes nonlinear effects, arbitrary initial conditions, and external strain forcing. Introducing the new generalized momentum coordinates (2.7) allowed a simple, linear expression for PV conservation in zero and uniform PV flow. Applying this conservation law, solutions for the cross-front streamfunction (2.30) and the buoyancy anomaly (2.26) were determined in terms of the along-front velocity. The frontogenesis problem was thus reduced to solving the differential equation in the along-front velocity (2.35). This equation contains two nonlinear terms, corresponding to vertical advection processes and a correction to the thermal wind, which were neglected to obtain a more tractable, approximate equation (2.38).

While the problems of deformation-forced frontogenesis and spontaneous (or self-forced) frontogenesis have previously been studied mostly in isolation, the solution presented herein emphasizes the similarity of the two problems. Our model unifies the HB72 model which applies at large time (or small Rossby numbers) where the strain-induced flow dominates, and the B00 model which applies at small time (or

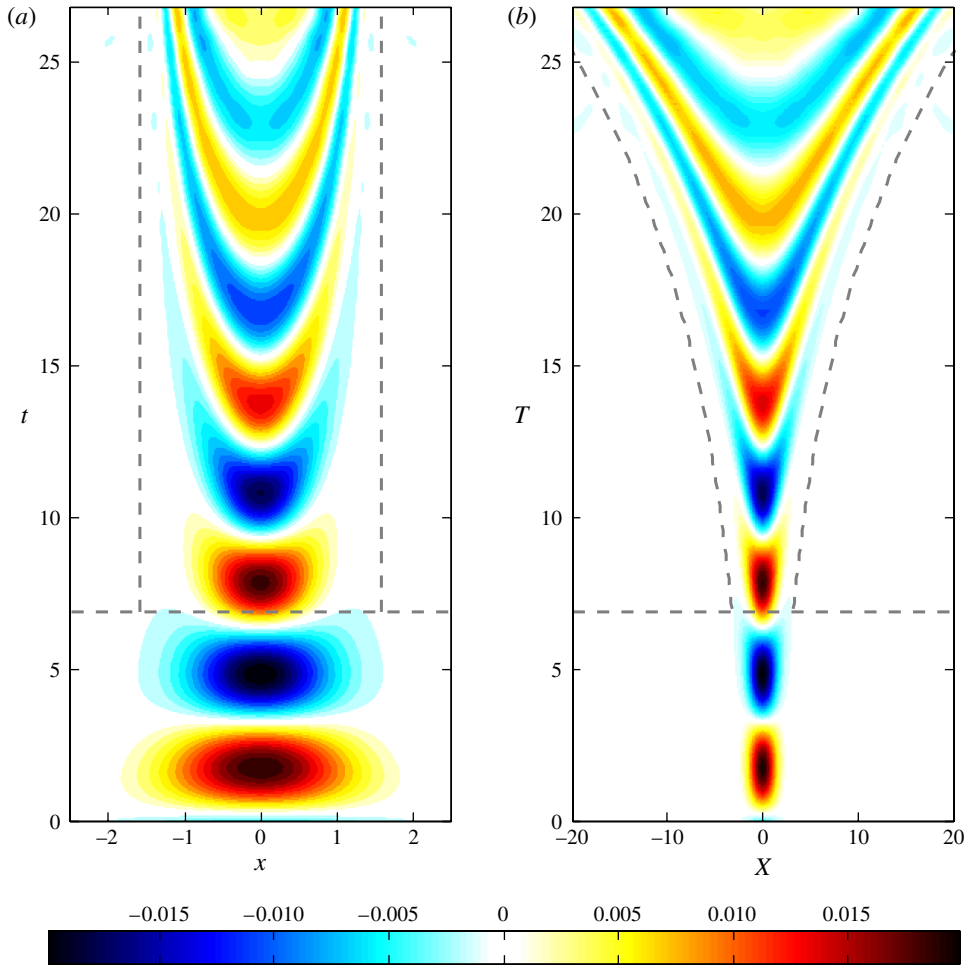


FIGURE 15. Hovmöller plot of the streamfunction difference $\psi - \psi_{HB}$ for parameter values of $Ro = 0.4$, $F = 0.8$ and $\delta = 0.1$, and unbalanced initial conditions, at height $z = 0.5$ in Eulerian coordinates (a) and momentum coordinates (b). Waves generated by the initial conditions are initially trapped until the release time $T_R \sim 7$ (shown as a horizontal dashed line) as non-decaying inertial oscillations. Once released the waves propagate towards a stagnation point $x_s = \pm 1.6$ shown by the vertical dashed line (a) and the dashed curve (b, $X_s = \pm x_s \exp \delta T$).

large Rossby numbers) where the oscillatory response of the system dominates. This generalization of the two models is most apparent in the predictions of critical time emerging from each model. Figure 16 displays the predicted critical time over the parameter space of the system for the generalized model formulated herein (solid), the HB72 model (dashed) and the B00 model (dot-dashed). As expected, the generalized solution approaches the corresponding HB72 solution in the small Rossby number limit and the B00 solution in the large Rossby number limit. The transition between the two solutions occurs near the critical Rossby number ($Ro_c = 2.03$ in the case shown). Our model thus provides a framework to study forced frontogenesis beyond the limits of the semigeostrophic approximation made by HB72 – that is, in cases where both strain and oscillatory effects are important. It is anticipated that this model

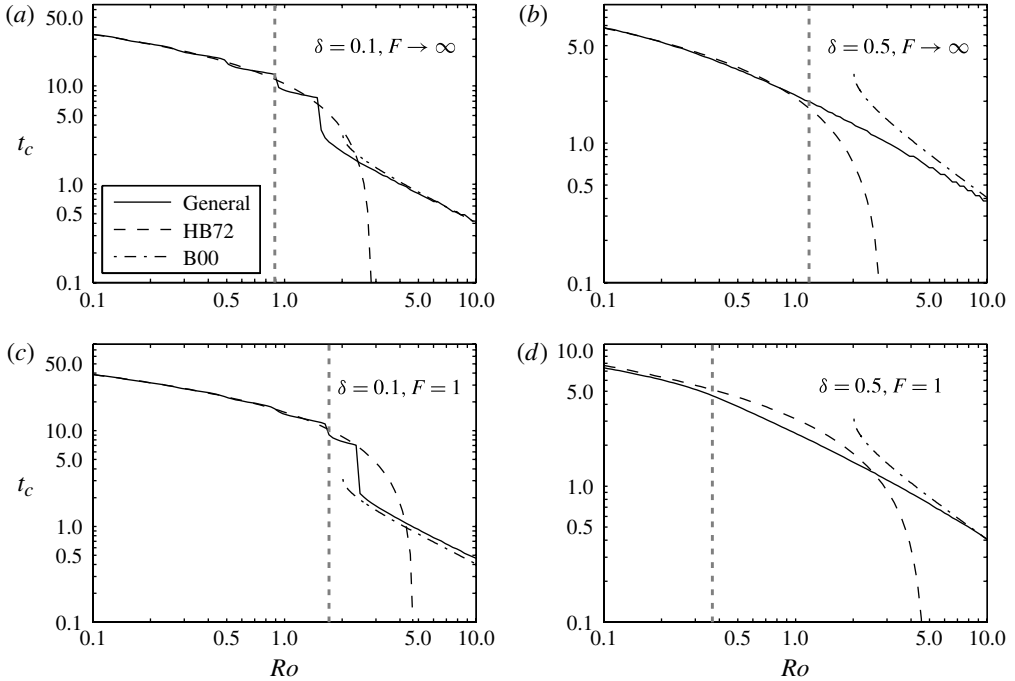


FIGURE 16. The variation of the non-dimensional critical time with Rossby number Ro for Froude numbers of $F \rightarrow \infty$ (a,b) and $F = 1$ (c,d), and strains of $\delta = 0.1$ (a,c) and $\delta = 0.5$ (b,d), as derived from the generalized model (2.38). The critical times predicted by the HB72 model (dashed) and B00 model (dot-dashed) are also shown. The assumed initial conditions are zero motion ($u = v = w = 0$) and an error function buoyancy profile (3.12) with critical Rossby number $Ro_c = 2.03$. The Rossby number at which the error in the HB72 prediction of the critical time first exceeds 10% is shown by a vertical dashed line. Since the size of the Rossby number controls the magnitude of the (near-inertial) oscillations in the frontal zone, a small increase in the Rossby number can cause the critical time to decrease by an entire inertial period, giving rise to the step-like features seen in the figure.

will be useful in analysing frontogenesis in geophysical flows such as the atmospheric mesoscale and ocean submesoscale, where Rossby numbers are of order unity and the initial flow may not be in geostrophic balance.

We also determined the nonlinear, time-dependent, analytic solution for the response of an initially motionless, uniformly stratified, rotating fluid to an unbalanced horizontal buoyancy gradient – that is, the uniform PV mass imbalance problem. Previously, only the adjusted state for this problem had been analytically determined (Blumen & Wu 1995). The key innovation allowing the solution to be found was the inclusion of an explicitly time-dependent anomaly term in the buoyancy field which encapsulates the extra complexity of uniform PV as compared with zero PV flow – or more generally, it becomes significant when the scale of the flow is small compared with the Rossby radius. The buoyancy anomaly accounts for the interaction between the pressure and momentum fields (the interchange of potential and kinetic energies) that permits the propagation of inertia–gravity waves. These waves are responsible for the adjustment of the initial mass imbalance to a geostrophically balanced state (which agrees with that derived by Blumen & Wu (1995)). There are three major results emerging from this solution.

First, the existence of an adjusted state does not imply attainability of that state, since the maximum flow gradients and minimum frontal width occur during the transient phase of the motion prior to the generation of inertia–gravity waves and associated energy loss from the frontal zone (as suggested by Plougonven & Zeitlin (2005)). Second, we determined (see figure 3) whether a frontal discontinuity will result for a given set of flow parameters (i.e. a given Rossby and Froude number). Our criterion is consistent with previous frontogenesis predictions empirically determined from numerical simulations (Neves 1996). Figure 3 demonstrates that the formation of a discontinuity is intrinsically linked to the propagation properties of inertia–gravity waves. Stronger background stratification (smaller Froude number) implies faster wave propagation and thus more rapid energy loss from the frontal zone, and a greater initial imbalance (larger Rossby number) is therefore required to generate a discontinuity. For sufficiently large background stratification we predict that the formation of a discontinuity is prohibited regardless of the size of the initial imbalance.

Third, our model provides a quantitative description of the dynamics of small-scale geostrophic adjustment. The key feature that emerges from this analysis is that an initial mass imbalance triggers the production of outward propagating inertia–gravity waves. The high wavenumber modes leave the imbalance region relatively quickly, leaving behind the near-inertial lower wavenumber modes and slowly decaying near-inertial oscillations (e.g. see the Hovmöller plot in figure 6). The extent and speed of geostrophic adjustment of the buoyancy field during this process is dependent on the size of the Burger number.

The dynamics of inertia–gravity wave generation and propagation in the presence of a strain field was also examined. In contrast to the unstrained case, where waves propagate freely out to infinity, in the strained case waves generated by the initial conditions are trapped for a finite period of time as non-decaying inertial oscillations in the frontal zone. The trapping time is greater for larger values of strain and smaller Burger numbers. Upon release the waves propagate away from the front with a decaying amplitude, shrinking horizontal scale, and ever-decreasing propagation speed. The waves become stationary at a fixed distance from the front, where their outward group velocity matches the inward strain flow velocity. These dynamics are graphically summarized by the Hovmöller plot shown in figure 15.

There are a number of caveats on our model. Firstly, the solutions presented herein only apply in the hydrostatic limit, although the model is open to generalization to non-hydrostatic flow. Secondly, the nonlinear terms in the momentum coordinate governing equation (2.35) were neglected in our solutions. These terms become important as the critical time is approached (see the Appendix) and could potentially provide a mechanism to arrest frontogenesis. Thirdly, the model is quasi-two-dimensional with gradients in the along-front direction neglected and thus the results only apply to sufficiently straight and long fronts. It is well known that even initially straight fronts can become deformed by eddies and large-scale flow. Also, frontal configurations predicted by the quasi-two-dimensional model may be unstable to small three-dimensional perturbations (e.g. McWilliams & Molemaker 2009, 2011). In such situations our results will only be applicable at times small compared with the time scales of these effects. Lastly, we observe that the momentum coordinates employed herein become invalid everywhere at the time of discontinuity formation since the inverse Jacobian of the coordinate transformation vanishes. Some attempts have been made to extend similar momentum coordinate solutions beyond this point, e.g. Cullen & Purser (1984), Koshyk & Cho (1992), and references therein.

Despite these limitations, the present model provides a framework to study the eventual fate of fronts. The prediction of a frontal discontinuity by our solutions does not necessarily imply that the system will approach such a state. In practice, neglected factors will become important when velocity and buoyancy gradients become sufficiently large. The evolving front may break down through hydrodynamic instabilities prior to the formation of a singularity in the model solution (e.g. McWilliams & Molemaker 2009), or an advective–diffusive balance (Blumen 1990) or frictional balance (Twiggs & Bannon 1998) may be established in the frontal zone. The solutions described here could be used to identify which neglected factors become important near the time of frontal collapse. Ultimately, this might provide insight into the physical mechanism responsible for the arrest of frontogenesis and the properties of equilibrated fronts. These issues will be addressed in a future study.

Acknowledgements

The authors gratefully acknowledge three reviewers whose constructive comments improved the quality and rigour of the manuscript. We also thank L. Thomas, A. Stewart, R. Plougonven and P. Haynes for many helpful discussions and comments. C.J.S. was supported by a Gates Cambridge Scholarship.

Appendix. Linearization error

Here we assess the error made in the neglect of the nonlinear terms in (2.35) and the validity of the linearized solution given by (2.38). The two nonlinear terms are the vertical advection term $-\mathcal{N}^*$, defined by (2.21), and the geostrophic velocity error Δv_g^* , defined by (2.12). To estimate the error introduced by the linearization we use an *a posteriori* analysis, using the linearized solution to compute the neglected terms. However, there is a complication in that the nonlinear terms involve second-order (and higher) vertical derivatives of the along-front flow (i.e. $\partial_{ZZ}v$), but the Fourier solution for v (e.g. (4.8a)) is $O(1/n^2)$. As a result, the Fourier series solution for the second- and higher-order derivatives is not convergent. We therefore choose to maintain the complex Fourier transform in X of (2.38), but take a vertical Chebyshev transform in $Z' = 2Z - 1$ instead of the Fourier cosine transform employed previously. As already noted, rigid lid boundary conditions require that the integral

$$\int_0^Z v \, dZ \sim w_* \tag{A 1}$$

vanish at the boundaries $Z = 0, 1$ (or $Z' = -1, 1$). We thus define vertical eigenfunctions ϕ_n satisfying relation (A 1) as follows:

$$\phi_n(Z') = \begin{cases} T_n(Z') & n = 1, \\ T_n(Z') + \frac{1 + (-1)^n}{2(n+1)(n-1)} & n \geq 2, \end{cases} \tag{A 2}$$

where T_n is the n th Chebyshev polynomial of the first kind. Transforming the linearized equation (2.38) into the above basis yields a set of $2N_k N_n$ coupled first-order equations in time, where N_k is the number of horizontal modes and N_n is the number of vertical modes. This equation set is solved numerically in MATLAB and agreement with the Fourier solution presented in the text is confirmed. The nonlinear terms are then computed using the velocity/buoyancy fields arising from this

linearized solution. The linearized solution is considered to break down if and when the nonlinear terms become of first-order importance.

The relative sizes of the nonlinear terms with time are displayed in figure 17 for six different sets of parameter values (Ro , Bu , δ) and unbalanced initial conditions. The quantity displayed is the maximum value of the nonlinear term at a given time scaled by the maximum value of the baroclinic part of the linear geostrophic velocity (the first term in (2.11)) at that time. Note that (as discussed in the text) the nonlinear geostrophic velocity Δv_g^* is identically zero for $Bu = 0$ and so is not shown in these cases. The frontal width parameter d (3.14) is also shown in grey in figure 17 to indicate the strength of the front at each time.

First consider the strain-forced cases (figure 17*a,c*), which both have $Ro = 1$ and $\delta = 0.1$ but different Bu . In both these cases the nonlinear terms remain less than $\sim 12\%$ of the linear terms until very close to the critical time. Figure 17*e* displays a non-frontogenetic, geostrophically adjusting ($\delta = 0$) case with $Ro = Bu = 2$. The estimated maximum error in neglecting the nonlinear terms in this case is less than 25% (and occurs at the time of minimum frontal width, labelled T_1). The size of both nonlinear terms then trends to zero as the system adjusts towards the steady state, since both the vertical velocity w and the ageostrophic along-front flow vanish in this state. Figure 17*b* shows a non-frontogenetic case without stratification or strain (e.g. as per the B00 model) having $Ro = 1$ and $Bu = 0$. The smaller Rossby number ($Ro = 1$, as compared with $Ro = 2$ for figure 17*e*) means that the maximum value of the error is smaller (less than 6%) but varies periodically with the inertial period since $Bu = 0$ and there is no wave propagation.

Lastly, consider figure 17*d,f*), which displays strain-free ($\delta = 0$) frontogenetic cases both with $Ro = 2.2$, but different Bu . The combination of the larger Ro (larger imbalance) and smaller Bu (slower wave propagation) leads to larger errors in these cases, but the error still remains less than $\sim 30\%$ for times $T < 0.8T_c$, where T_c is the critical time. Note that figure 17*f*) is an estimate of the error in the B00 solution (with zero PV) due to the neglect of vertical advection effects. A numerical study by Blumen & Williams (2001) demonstrated that the inclusion of these effects results in (i) an increase in the critical Rossby number, Ro_c , and (ii) an increase in the time taken for frontogenesis.

Figure 18 displays the spatial structure of the nonlinear terms for figure 17*e*) at the time of minimum frontal width T_1 . The buoyancy contours are overlaid in grey to show the location of the front. The maximum magnitude of the geostrophic velocity term, Δv_g^* , occurs on the boundary at the location of the front, whereas the vertical advection term, \mathcal{N}^* , is largest on the boundary both at the location of the front and behind the front. The vertical advection term also has a significant interior signal associated with wave generation, and this signal follows the waves as they propagate outwards.

Figure 19 displays the spatial structure of the nonlinear terms for figure 17*a*) just prior to the critical time, again with buoyancy contours overlaid in grey. The geostrophic velocity term is maximized just behind the (near-discontinuous) front where horizontal velocity gradients are largest. The vertical advection term is largest in a thin along-isopycnal strip directly above (or below) the surface front, where vertical velocities are predicted to be largest.

Given the above results, the linearized solution presented in the text is expected to be a reasonable approximation in most cases until near to the time of predicted discontinuity formation, at which point the neglected nonlinear terms contribute at

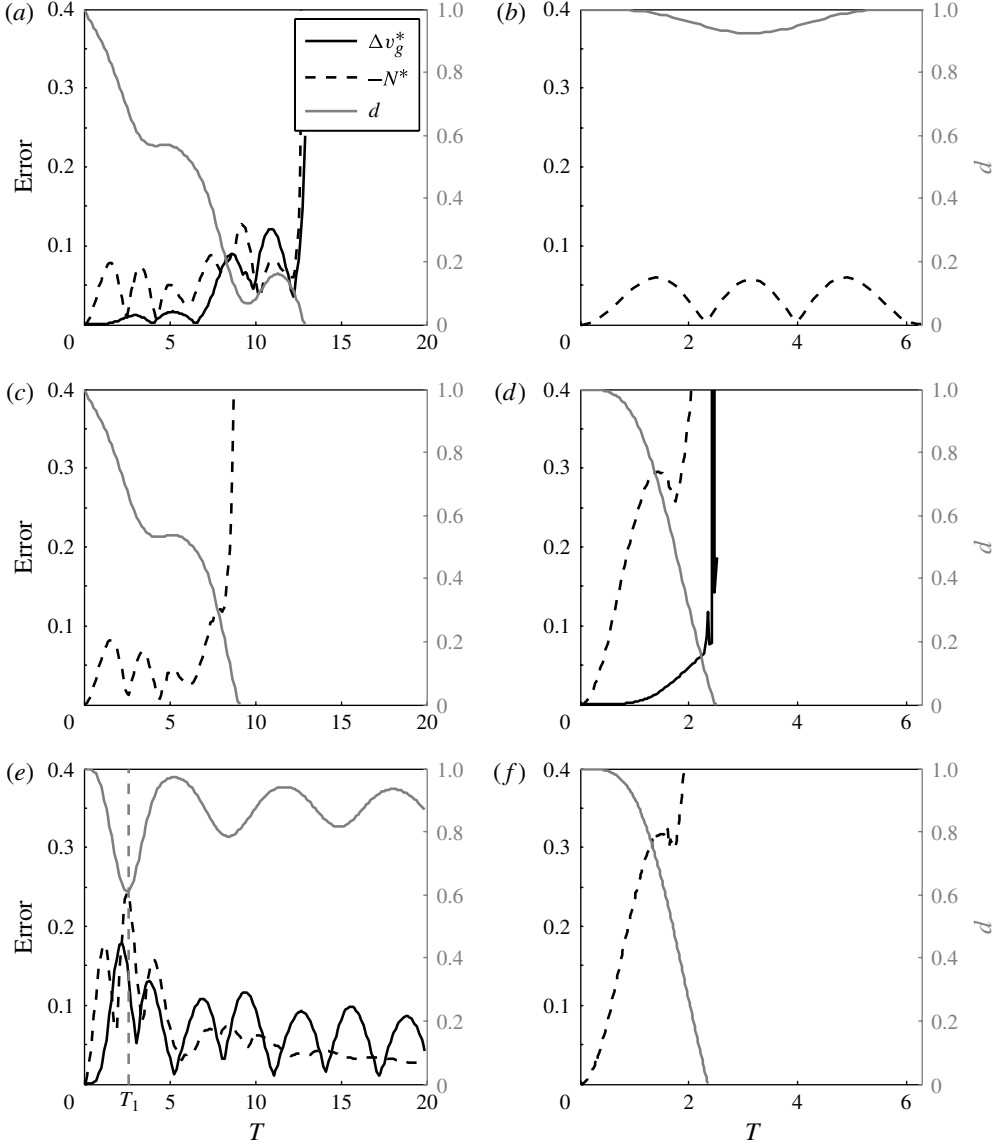


FIGURE 17. The time evolution of the maximum magnitude of the nonlinear terms in (2.35), $-\mathcal{N}^*$ (dashed black) and Δv_g^* (solid black), relative to the maximum magnitude of the linearized geostrophic velocity (2.11), as computed from the linearized solution (2.38) for a spread of parameter values. The frontal width parameter d , defined by (3.14), is also shown in grey on the right-hand axis. The spatial structure of the nonlinear terms for (e) at the time marked T_1 (indicated by a vertical dashed grey line) is displayed in figure 18. The spatial structure of the nonlinear terms for (a) just prior to the critical time is displayed in figure 19: (a) $Ro = 1, Bu = 0.5, \delta = 0.1$; (b) $Ro = 1, Bu = 0, \delta = 0$; (c) $Ro = 1, Bu = 0, \delta = 0.1$; (d) $Ro = 2.2, Bu = 0.733333, \delta = 0$; (e) $Ro = 2, Bu = 2, \delta = 0$; (f) $Ro = 2.2, Bu = 0, \delta = 0$.

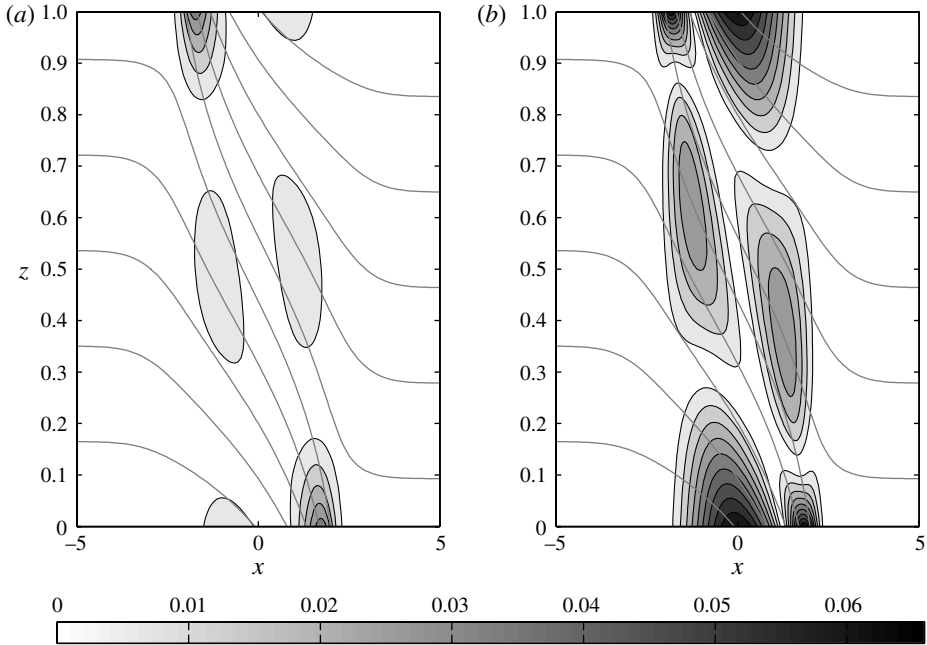


FIGURE 18. The spatial structure of the nonlinear terms Δv_g^* (a) and $-\mathcal{N}^*$ (b) in (2.35) for the case with $Ro = Bu = 2$ and $\delta = 0$ at time $T_1 = 2.8$ (see figure 17e), as computed from the linearized solution (2.38). Buoyancy contours are superimposed in grey.

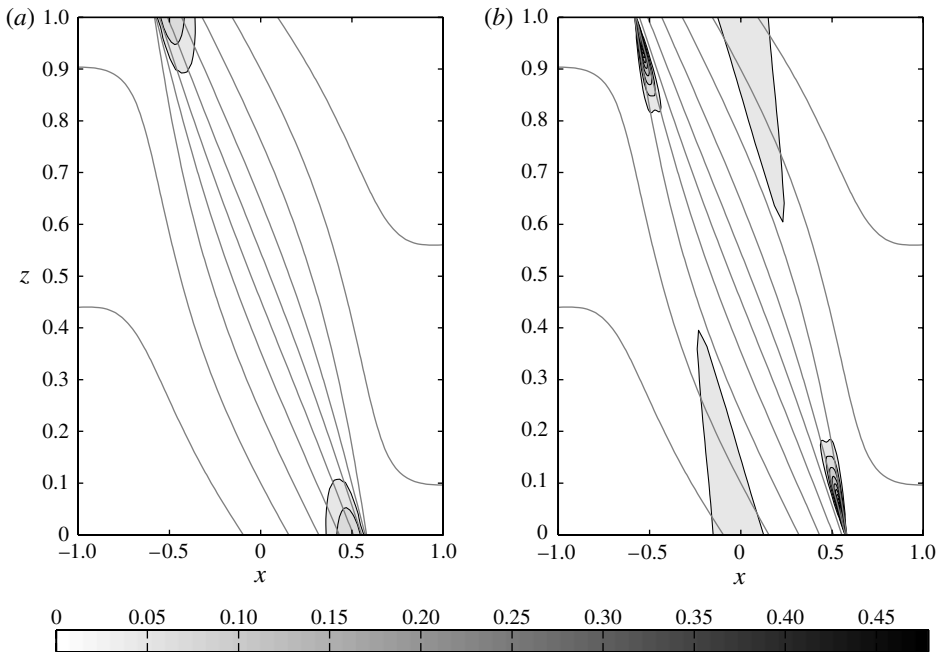


FIGURE 19. The spatial structure of the nonlinear terms Δv_g^* (a) and $-\mathcal{N}^*$ (b) in (2.35) for the case with $Ro = 1$, $Bu = 0.5$ and $\delta = 0.1$ just prior to the critical time (see figure 17a), as computed from the linearized solution (2.38). Buoyancy contours are superimposed in grey.

leading order. A more precise evaluation of the influence of the neglected terms could be made using a fully nonlinear numerical solution – a topic left for a future work.

REFERENCES

- BLUMEN, W. 1972 Geostrophic adjustment. *Rev. Geophys. Space Phys.* **10**, 485–528.
- BLUMEN, W. 1990 A semigeostrophic Eady-wave frontal model incorporating momentum diffusion. Part 1. Model and solutions. *J. Atmos. Sci.* **47**, 2890–2902.
- BLUMEN, W. 1997 A model of inertial oscillations with deformation frontogenesis. *J. Atmos. Sci.* **54**, 2681–2692.
- BLUMEN, W. 2000 Inertial oscillations and frontogenesis in a zero potential vorticity model. *J. Phys. Oceanogr.* **30**, 31–39.
- BLUMEN, W., GAMAGE, N., GROSSMAN, R. L., LEMONE, M. A. & MILLER, L. J. 1996 The low-level structure and evolution of a dry arctic front over the central United States. Part 2. Comparison with theory. *Mon. Weath. Rev.* **124**, 1676–1691.
- BLUMEN, W. & WILLIAMS, R. T. 2001 Unbalanced frontogenesis. Part 1. Zero potential vorticity. *J. Atmos. Sci.* **58**, 2180–2195.
- BLUMEN, W. & WU, R. 1995 Geostrophic adjustment: frontogenesis and energy conversion. *J. Phys. Oceanogr.* **25**, 428–438.
- BOCCALETTI, G., FERRARI, R. & FOX-KEMPER, B. 2007 Mixed layer instabilities and restratification. *J. Phys. Oceanogr.* **37**, 2228–2250.
- BOUCHUT, F., SOMMER, J. & ZEITLIN, V. 2004 Frontal geostrophic adjustment and nonlinear wave phenomena in one-dimensional rotating shallow water. Part 2. High-resolution numerical simulations. *J. Fluid Mech.* **514**, 35–63.
- BRETHERTON, F. P. & GARRETT, C. J. R. 1969 Wave trains in inhomogeneous moving media. *Proc. R. Soc. A* **302**, 529–554.
- BUHLER, O. & MCINTYRE, M. E. 2005 Wave capture and wave-vortex duality. *J. Fluid Mech.* **534**, 67–95.
- CULLEN, M. & PURSER, R. 1984 An extended theory of semigeostrophic frontogenesis. *J. Atmos. Sci.* **41**, 1477–1497.
- DAVIES, H. C. & MULLER, J. C. 1988 Detailed description of deformation-induced semi-geostrophic frontogenesis. *Q. J. R. Meteorol. Soc.* **114**, 1201–1219.
- ELIASSEN, A. 1959 On the formation of fronts in the atmosphere. In *The Atmosphere and Sea in Motion* (ed. B. Bolin), Rockefeller Institute Press.
- ELIASSEN, A. 1962 On the vertical circulation in frontal zones. *Geophys. Publ.* **24** (4), 147–160.
- FERRARI, R. 2011 A frontal challenge for climate models. *Science* **332** (6027), 316–317.
- HOSKINS, B. J. 1982 The mathematical theory of frontogenesis. *Annu. Rev. Fluid Mech.* **14**, 131–151.
- HOSKINS, B. J. & BRETHERTON, F. P. 1972 Atmospheric frontogenesis models: mathematical formulation and solution. *J. Atmos. Sci.* **29**, 11–37.
- KOSHYK, J. N. & CHO, H. 1992 Dynamics of a mature front in a uniform potential vorticity semigeostrophic model. *J. Atmos. Sci.* **49** (6), 497–510.
- MAHADEVAN, A., D’ASARO, E., LEE, C. & PERRY, M. J. 2012 Eddy-driven stratification initiates North Atlantic spring phytoplankton blooms. *Science* **337** (6090), 54–58.
- MCWILLIAMS, J. C. & MOLEMAKER, M. J. 2009 Linear fluctuation growth during frontogenesis. *J. Phys. Oceanogr.* **39**, 3111–3129.
- MCWILLIAMS, J. C. & MOLEMAKER, M. J. 2011 Baroclinic frontal arrest: a sequel to unstable frontogenesis. *J. Phys. Oceanogr.* **41**, 601–619.
- NEVES, A. 1996 Unbalanced frontogenesis with constant potential vorticity. Master’s thesis, Naval Postgraduate School, Monterey, California.
- OSTDIEK, V. & BLUMEN, W. 1997 A dynamic trio: inertial oscillation, deformation frontogenesis, and the Ekman–Taylor boundary layer. *J. Atmos. Sci.* **54**, 1490–1502.
- OU, H. W. 1984 Geostrophic adjustment: a mechanism for frontogenesis. *J. Phys. Oceanogr.* **14**, 994–1000.

- PLOUGONVEN, R. & ZEITLIN, V. 2005 Lagrangian approach to geostrophic adjustment of frontal anomalies in stratified fluid. *Geophys. Astrophys. Fluid Dyn.* **9**, 101–135.
- ROSSBY, C. G. 1938 On the mutual adjustment of pressure and velocity distributions in certain simple current systems. Part 2. *J. Mar. Res.* **1**, 239–263.
- SAWYER, J. S. 1956 On the vertical circulation at meteorological fronts and its relation to frontogenesis. *Proc. R. Soc. Lond. Ser. A* **234**, 346–362.
- SNYDER, C., SKAMAROCK, W. & ROTUNNO, R. 1993 Frontal dynamics near and following frontal collapse. *J. Atmos. Sci.* **50**, 3194–3211.
- TANDON, A. & GARRETT, C. 1994 Mixed layer restratification due to a horizontal density gradient. *J. Phys. Oceanogr.* **24** (6), 1419–1424.
- TAYLOR, J. R. & FERRARI, R. 2011 Ocean fronts trigger high latitude phytoplankton blooms. *Geophys. Res. Lett.* **38**, L23601.
- THOMAS, L. N. 2012 On the effects of frontogenetic strain on symmetric instability and inertia–gravity waves. *J. Fluid Mech.* **711**, 620–640.
- THOMAS, L. N. & JOYCE, T. M. 2010 Subduction on the northern and southern flanks of the gulf stream. *J. Phys. Oceanogr.* **40** (2), 429–438.
- THOMAS, L. N., TANDON, A. & MAHADEVAN, A. 2008 Submesoscale processes and dynamics. In *Geophysical Monograph Series 177: Ocean Modelling in an Eddying Regime*. American Geophysical Union.
- THOMAS, L. N., TAYLOR, J. R., FERRARI, R. & JOYCE, T. M. 2013 Symmetric instability in the gulf stream. *Deep-Sea Res. II* **91**, 96–110.
- TWIGG, R. D. & BANNON, P. R. 1998 Frontal equilibration by frictional processes. *J. Atmos. Sci.* **55**, 1084–1087.
- WU, R. & BLUMEN, W. 1995 Geostrophic adjustment of a zero potential vorticity flow initiated by a mass imbalance. *J. Phys. Oceanogr.* **25**, 439–445.